Heavy Rydberg states

Reinhold, E.M.; Ubachs, W.M.G.

published in
Molecular Physics
2005

DOI (link to publisher)
10.1080/00268970500050621

document version
Publisher's PDF, also known as Version of record

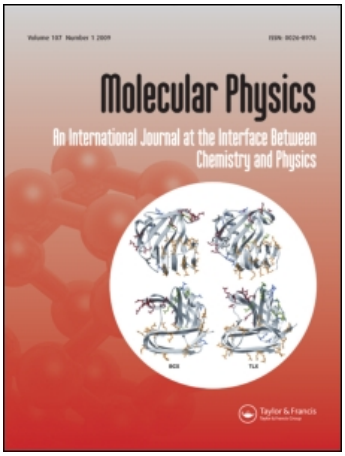

Molecular Physics
Publication details, including instructions for authors and subscription information:
http://www.informaworld.com/smpp/title~content=t713395160

Heavy Rydberg states

Elmar Reinhold[a]; Wim Ubachs[b]
[a] Laboratoire Aimé Cotton, Université de Paris-Sud, 91405 Orsay, France [b] Laser Centre, Department of Physics and Astronomy, Vrije Universiteit, De Boelelaan 1081, 1081 HV Amsterdam, The Netherlands

To cite this Article Reinhold, Elmar and Ubachs, Wim(2005) 'Heavy Rydberg states', Molecular Physics, 103: 10, 1329 — 1352
To link to this Article: DOI: 10.1080/00268970500050621
URL: http://dx.doi.org/10.1080/00268970500050621

Molecular Physics, Vol. 103, No. 10, 20 May 2005, 1329–1352

Taylor & Francis
Taylor & Francis Group

Heavy Rydberg states

ELMAR REINHOLD† and WIM UBACHS‡*

†Laboratoire Aimé Cotton, Université de Paris-Sud, 505 Campus d'Orsay, 91405 Orsay, France
‡Laser Centre, Department of Physics and Astronomy, Vrije Universiteit, De Boelelaan 1081, 1081 HV Amsterdam, The Netherlands

(*Received 21 September 2004; in final form 10 January 2005*)

This paper discusses the nature of heavy Rydberg states, i.e. quantum states in molecular systems that are bound by the almost pure Coulomb potential between pairs of ions. A theoretical framework is developed in terms of mass-scaling laws for heavy Rydberg systems of certain reduced mass, so that the physics of electronic Rydberg states can be straightforwardly applied to heavier ion-pair systems, or any other system bound by a $1/r$ potential. The general description of such quantum systems is supported by an experimental investigation of the energy region near the H^+H^- ion-pair dissociation limit, using a 1 XUV + 1 UV laser excitation scheme. Such a scheme allows for preparation of a single intermediate rovibrational quantum state, from which the ion-pair threshold region can be explored with a narrowband Fourier-transform limited laser. Field-induced lowering of the H^+H^- dissociation limit was observed in the presence of an electric field. Using a combination of DC and pulsed electric fields two-photon induced threshold ion-pair production spectroscopy (TIPPS) was performed for a variety of field strengths. Below the field-dissociation limit coherent wave packets of bound heavy Rydberg states are excited in an electric field. The coherent evolution of the Stark states, giving rise to oscillations in angular momentum space, can be quantitatively understood in terms of the linear Stark effect in the hydrogen atom, where the light electron is replaced by the heavier H^- particle. The dynamics of wave packets of heavy Rydberg states is slower than in ordinary electronic Rydberg states, according to their larger mass. For a wide variety of binding energy and external electric field, the observed oscillation frequencies of the Stark wave packets match this model. An important parameter describing the specific properties of the H^+H^- Rydberg states is the scaled lifetime, which may be considered as a material constant, and it is determined at $\tau = (5.8 \pm 2.0) \times 10^{-21}\,\mathrm{s}\,n^4$.

1. Introduction

From the perspective of electronic Rydberg structure all atoms and molecules are very much alike. A negatively charged electron is bound in the field of a positively charged ionic core, governed by Coulombic attraction with potential $V_C = -Ze^2/4\pi\epsilon_0 r$. The energies of bound levels in the Rydberg series is given by the Rydberg formula [1]

$$E_n = -\frac{R}{(n-\delta)^2}, \tag{1}$$

where R is the Rydberg constant, n is the principal quantum number and δ is the quantum defect. This equation holds for atoms and molecules; specific physical effects of the structure of the ionic core are entailed in the quantum defect. The Rydberg constant, given by

$$R_A = \frac{\mu}{2\hbar^2}\left(\frac{e^2}{4\pi\epsilon_0}\right)^2 = \frac{\mu}{m_e} R_\infty, \tag{2}$$

is nearly equal for all atoms and molecules, because $\mu/m_e = m_{A^+}/(m_{A^+} + m_e) \approx 1$, independent of the mass or the internal structure of the ionic core. As a consequence the level density of Rydberg levels, scaling with $1/n^3$, is the same in all cases. The dynamics of Rydberg states follows a general behaviour; the radiative lifetime scales with n^3, while in molecules the (pre)-dissociative and autoionizing dynamics is governed by the same n^3 scaling. Of course in complex atoms and in molecules the Rydberg structure tends to become complicated in view of the interactions between series converging to the several fine-structure and rovibrational states of the ionic core [2–4].

*Corresponding author. Email: wimu@nat.vu.nl

Molecular Physics
ISSN 0026–8976 print/ISSN 1362–3028 online
http://www.tandf.co.uk/journals
DOI: 10.1080/00268970500050621

Some variation in the value of the Rydberg constant is established in positronium (e^+e^-), where R is smaller by a factor of two, while in muonium (μ^+e^-) the value for R is already close to that of atoms. Ion-pair states in molecules open up a wide dynamical range for experimental studies of Rydberg systems. The Rydberg constant $R_{\text{ion-pair}} = (\mu/m_e)R_\infty$ is much larger than in the electronic case. Therefore the level structure in each ion-pair molecular system depends on the reduced mass of the system, in which there is a large variety. For the lightest of such systems, the H^+H^- ion-pair system studied in this work, the reduced mass is $\mu = (1/2)M_H$, where M_H is the mass of the hydrogen atom, therewith increasing the Rydberg constant by three orders of magnitude. For heavier molecules, including polyatomic ones, further increase of the value of R can be established. The ion-pair limit in H^+H^- is special in the sense that there is only a single limit, even when the finest detail is considered. Both particles have no substructure; for the proton this is obvious but also for H^- this is the case, since it can exist only in the $^1S_0$ ground state, which has no fine nor hyperfine structure.

Coulomb potentials of ion-pair systems can also be viewed as a class of molecular potentials describing an ionic bond. A remarkable difference from other molecular potentials is the infinite number of bound states of nuclear motion (ro-vibrational states) supported close to the dissociation threshold; potentials associated with a covalent bond typically show an asymptotic shape of $V_n \sim 1/r^n$ with $n = 3$–6 and consequently support a finite number of bound states. A connection between the standard treatment of molecules on the one hand, using potentials of electronic states and quantized nuclear motion described by vibrational and rotational quantum numbers v and J, and an ion-pair Rydberg model on the other was established [5]:

$$n \leftrightarrow v + J + 1 \tag{3}$$

with v and J the common quantum numbers for vibration and angular momentum (rotation). The issue of the large quantum defect associated with heavy Rydberg systems will be discussed below.

Chupka *et al.* [6] investigated the process of ion-pair formation in H_2, HD and D_2, using a classical spectrometer. It was found that the threshold region is a structured continuum with characteristic window resonances superimposed. These resonances are states belonging to Rydberg series converging to the $X^1\Sigma_g^+$, $v^+ = 9$, $N = 2$ limit in the H_2^+ ion, that undergo predissociation as well as autoionization. The underlying unresolved structure relates to overlapping resonances converging to $v^+ = 9$, $N = 0$. The electronic Rydberg structure was found to dominate the dynamics at excitation energies near the H^+H^- threshold. Above this threshold the H^- channel carries less than 1% of the signal, while autoionization dominates the ion production yielding H_2^+. Continuity of oscillator strength below and above a Rydberg limit then predicts that also in the energy region below the H^+H^- threshold, where bound H^+H^- states exist, the continua of $H_2^+e^-$ electronic Rydberg states dominate the spectrum. In the work of Kung *et al.* [7] a two-step excitation scheme was followed with laser preparation of a single rovibrational quantum state (either $B^1\Sigma_u^+$ or $C^1\Pi_u$) to reach the ion-pair limit. Both Rydberg series converging to the H_2^+, $v^+ = 9$, $N = 1$ and $N = 3$ limits were unravelled above the H^+H^- threshold with the improved resolution of the double resonance laser scheme. Pratt *et al.* [8] also performed two-step excitation, now using the $EF^1\Sigma_g^+$ state as intermediate. They demonstrated that the electric field-induced lowering of the saddle point in the case of H^+–H^- field dissociation follows the physical behaviour as in electronic ionization.

Martin and Hepburn demonstrated that just below the H^+H^- pair limit there exist long-lived states, particularly in the presence of an electric field. They exploited this property to develop the technique of threshold ion-pair production spectroscopy (TIPPS) and applied it to O_2 [9] and HCl [10]. Later TIPPS, which can be considered as the ion-pair analogue to zero electronic kinetic energy (ZEKE) spectroscopy for electronic Rydberg states [11], was also employed to study the H^+H^- threshold region in H_2 and D_2 [12]. Wang *et al.* [13] extended the threshold and TIPPS studies to halogen molecules, which in most cases have the advantage that the ion-pair limit is below the ionization potential thus avoiding parasitic ion signals from autoionization. The mechanism for excitation of ion-pair Rydberg states is in general an issue of debate; in the studies on ICl [13] and I_2 [14] the focus was on identifying 'doorway' states for ion-pair excitation. The same TIPPS technique was employed to probe ion-pair states of polyatomic molecules (H_2S), exhibiting a multitude of Rydberg limits and it was demonstrated that bond dissociation energies could be determined to high accuracies, based on the zero-ion kinetic energy measurements [15].

In principle the ion-pair Rydberg structure should be studied by probing the consecutive states in a series by frequency domain spectroscopy. Attempts to resolve the series were however unsuccessful for various reasons to be discussed. Alternatively sets of nearby lying states can be coherently excited, forming a localized and non-stationary wave function density. While Schrödinger had already eluded on the topic of coherent superposition of eigenstates in 1926 [16], Zoller and

co-workers proposed a scheme for generating electron wave packets with laser pulses [17]. More than a decade ago the groups of Van Linden van den Heuvell [18, 19] and Stroud and co-workers [20, 21] successfully demonstrated the excitation of localized electron wave packets. The time-dependent oscillatory behaviour of the wave packets was probed in terms of revival of the electron density by removing the electron when returning to the ionic core by a pulsed laser on the picosecond time scale. Use was made of the property that the recoil momentum of the electron in the ionization process can only be absorbed by the ionic core if the electron returns to this core. In the experiments radially (several n states coherently excited) as well as angularly (several ℓ or k Stark states coherently excited in an electric field) localized electron wave packets were studied. Wave packets of the nuclear motion in molecules have been investigated by a large number of groups; we mention here the work of Zewail and co-workers, who coherently excited vibrational and rotational wave packets in the I_2 molecule [22]. In recent years investigations with such wave packets have become established methods and form the basis of the new field of femto-chemistry [23].

In the experiment presented here the Rydberg-like structure of the heavy ion-pair system H^+H^- is revealed by preparing coherent superpositions of (n, k) states in an electric field. In fact the analogous study for electronic Rydberg states in an electric field had been performed by Lankhuizen and Noordam [24]; an atomic streak camera had to be implemented to follow the fast dynamics. Since the dynamics of the ion-pair Rydberg states is much slower due to the heavier mass of the particle in the $1/r$ potential, the temporal dynamics can be probed on a nanosecond time scale using pulsed electric fields with slower rise-times. A preliminary report on the observation of coherent Stark wave packets in heavy Rydberg systems has been published previously [25].

2. Theory

2.1. *Covalent and ion-pair potentials in H_2*

One way to classify bound molecular electronic states is the type of fragments into which the molecule separates at large internuclear distance: neutral atoms for a covalent bond, and an ion pair for an ionic bond. In the region of relatively small internuclear distances ($R < 10$ au) the ion-pair Coulombic potential interacts with the covalent states, giving rise to a variety of bound electronic states with more or less ionic character in different intervals of R.

For the H_2 system the outer wells of the lowest excited states $B\,^1\Sigma_u^+$ and $EF\,^1\Sigma_g^+$ closely follow the ion-pair potential. The same is true for some higher lying long-range states, that were recently observed in multiple resonance excitation schemes: the $H\bar{H}\,^1\Sigma_g^+$ [26] and $B''\bar{B}\,^1\Sigma_u^+$ [27] states. Such states can be considered as precursors to ion-pair or heavy Rydberg states in the region of low principal quantum number.

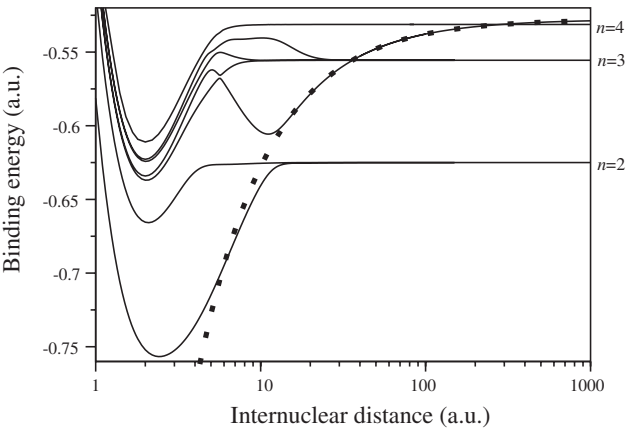

Figure 1. Some of the $^1\Sigma_u^+$ molecular potentials in H_2, which have a part ion-pair character or interact with these. A similar manifold exists for $^1\Sigma_g^+$ (see figure 12) as well as for Π states. The dotted line indicates a pure Coulomb potential for H^+H^-; potentials correlating with the $n = 2$ and $n = 3$ dissociation limits are taken from [28], while the uppermost curve only represents schematically the states that correlate with $n = 4$ dissociation. A logarithmic scale for internuclear distance allows one to simultaneously show details at long and short range.

In figure 1 the potential energy curves of $^1\Sigma_u^+$ states are shown as obtained in *ab initio* calculations by Wolniewicz and Staszewska [28]. Similar sets of potentials of $^1\Sigma_g^+$ and higher orbital angular momentum projections ($^1\Pi_u$, $^1\Pi_g$, etc.) exist. An important characteristic of the electronically excited states is the formation of double-well potentials in the hydrogen molecule. These double-well potentials result from interaction between Rydberg states and repulsive doubly-excited states (at short internuclear distance R where molecular electronic configurations prevail) and between covalent and ionic states (at larger R where electronic states are more atom-like).

Detmer *et al.* [29] and Staszewska and Wolniewicz [28, 30] have investigated some higher lying double well states of $^1\Sigma_u^+$ and $^1\Sigma_g^+$ symmetry correlating with the $(n = 3)$ and $(n = 4)$ dissociation limits. These states follow almost exactly the ion-pair potential in large parts of their outer limbs. The issue whether the outer wells of e.g. the $6\,^1\Sigma_u^+$ state supports bound states was recently addressed by Koelemeij *et al.* [31]. It was argued that the predissociative decay as a result from Landau–Zener transitions at the point where the ion-pair potential crosses the energetic region of the $(n = 3)$

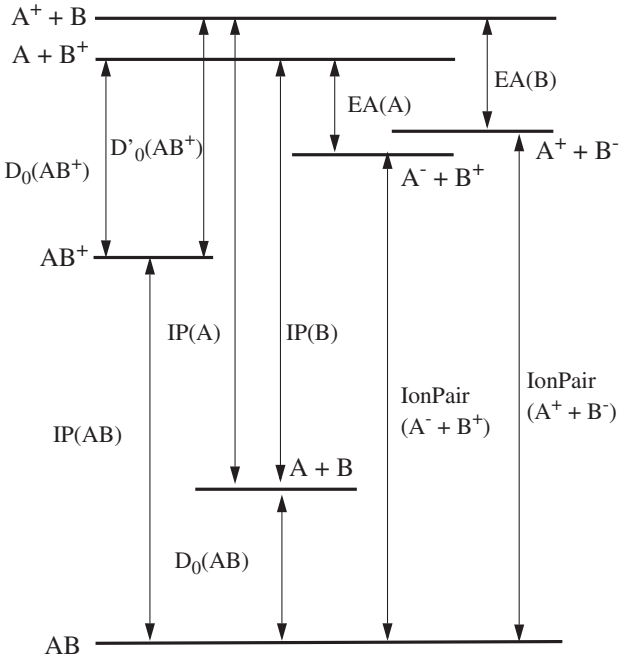

Figure 2. Thermodynamic cycle representing relations between ionization potentials, dissociation energies, ion-pair thresholds and electron affinities for a heteronuclear diatomic AB.

dissociation limit, at internuclear separation of 22 au with an avoided crossing split by only $60\,\mathrm{cm}^{-1}$, may cause all lines to broaden to the extent that spectral structure is lost. In a search for bound levels in $6\,^1\Sigma_u^+$ indeed none were found. It may be expected that for heavy Rydberg states in the region of the crossing the $(n = 4)$ limit at 280 au predissociative coupling is essentially absent, because configuration interaction between neutral and ionic states should then be negligible; there are however no observations available. It should be noted that the ion-pair potential does not cross an infinite manifold of dissociation limits. In H_2 the ion-pair threshold is in between the $(n = 4)$ and $(n = 5)$ dissociation energies.

The effect of such decay processes on the stability of the H^+H^- state will be discussed in more detail in section 4.4.

2.2. *The ion-pair threshold and other characteristic energies*

The excitation energy of ion-pair limits for systems A^+B^- are connected, in thermodynamic cycles, to the values of the ionization potentials, both for the parent molecules as for the individual atoms, of the dissociation energies of the neutral molecule AB, as well for the ions, either A^+B or AB^+, and the electron affinities of the constituent atoms. In figure 2, a general picture of the thermodynamic cycles is displayed, which can be used to derive ion-pair thresholds, that are in many cases less well known than the ionization potentials. For the case of H^+H^- the most recent and accurate values for the relevant parameters are compiled in table 1. From figure 2, a value for the ion-pair threshold $IP(H^+H^-)$ then follows via:

$$IP(H^+H^-) = IP(H_2) + D_0(H_2^+) - EA(H) \qquad (4)$$

or via:

$$IP(H^+H^-) = D_0(H_2) + IP(H) - EA(H), \qquad (5)$$

whichever is most accurate. Experimentally no direct values for the dissociation energies of the ions have been determined. The values, listed as experimental (see [35, 36]) for $D_0(H_2^+)$ are derived from dissociation energies of the neutral molecule and involve ionization potentials of the atoms. Therefore equation (5) is used to derive a value for the ion-pair threshold. The thermodynamic cycles can be used to determine electron affinities from direct measurements of ion-pair thresholds. In the most recent and most accurate determination of the dissociation energy the fine and hyperfine splittings at threshold become resolved such that there is no longer a single value for the dissociation limit [36].

Table 1. Thermodynamic properties of the hydrogen atoms, molecules and ion-pair systems. All values in cm^{-1}.

H_2: ionization potential	124417.480(11)	[32, 33]
H_2: dissociation energy	36118.06(4)	[34–36]
H_2^+: dissociation energy	21379.343(14)	[35, 36]
H: ionization potential	109678.7712	[37]
H: electron affinity	6082.99(15)	[38]
H^+H^- ion-pair threshold	139713.83(16)	

2.3. *Mass scaling in the Rydberg manifolds*

The physical laws governing (electronic) Rydberg states can be put in simple form, expressing the dependence of the major physical quantities as a function of n, when scaled in so-called atomic units. These units are listed in table 2, with an expression in terms of fundamental constants $m_e, e, \hbar, \epsilon_0$ and c, along with the values of these constants in SI units. The quantities describing the physical properties of Rydberg systems, such as the binding energy $E(n)$, or the radius of a Kepler orbit $R(n)$ and so forth, are listed in table 3. The Stark splitting $\delta E_s(n, F)$ is expressed for an electric field F and represents the splitting between two adjacent Stark levels (usually denoted by their parabolic quantum numbers k) when only the linear Stark effect is included and quantum defects (δ in equation (1)) are neglected.

Table 2. Atomic units for electronic Rydberg systems and ion-pair units for heavy Rydberg systems. In the last column SI-values are given for the H^+H^- system with $M = 918.5761$. Note that the Rydberg constant is not the atomic unit of wave number, because its definition involves the speed of light, which is not the atomic unit of velocity.

Quantity	Symbol	Expression	SI value	IP units	SI value (H^+H^-)
Mass	m_e	m_e	9.109383×10^{-31} kg	$M\,m_e$	8.367662×10^{-28} kg
Action	$\hbar$	$\hbar$	1.054572×10^{-34} J s	$\hbar$	1.054572×10^{-34} J s
Charge	e	e	1.602177×10^{-19} C	e	1.602177×10^{-19} C
Time	τ_0	$(4\pi\epsilon_0)^2\hbar^3/m_e e^4$	2.418884×10^{-17} s	$M^{-1}\tau_0$	2.633297×10^{-20} s
Length	a_0	$4\pi\epsilon_0\hbar^2/m_e e^2$	5.291772×10^{-11} m	$M^{-1}a_0$	5.760842×10^{-14} m
Velocity	v_0	$e^2/4\pi\epsilon_0\hbar$	2.187691×10^6 m s^{-1}	v_0	2.187691×10^6 m s^{-1}
Energy	E_h	$m_e e^4/(4\pi\epsilon_0)^2\hbar^2$	4.359744×10^{-18} J	$M\,E_h$	4.004757×10^{-15} J
Potential	U_0	$m_e e^3/(4\pi\epsilon_0)^2\hbar^2$	27.211385 V	$M\,U_0$	24995.73 V
Electric field	F_0	$m_e^2 e^5/(4\pi\epsilon_0)^3\hbar^4$	5.142206×10^{11} V m^{-1}	M^2F_0	4.338901×10^{17} V m^{-1}
Magnetic field	B_0	$m_e^2 e^3/(4\pi\epsilon_0)^2\hbar^3$	2.350517×10^5 T	M^2B_0	1.9833324×10^{11} T
Rydberg constant	R_∞	$E_h/2hc$	1.097373×10^7 m^{-1}	$M\,R_\infty$	1.008021×10^{10} m^{-1}

The Inglis–Teller limit $F_{IT}(n)$ is defined as the electric field at which the width of an entire Stark manifold $\Delta E_s(n, F)$ reaches the Rydberg state splitting $\Delta E(n)$; at that field strength the lowest k Stark level, pertaining to the $(n+1)$-manifold has the same energy as the highest k level in the manifold with n.

Pure ion-pair states A^+B^- show a similar physical behaviour as electronic Rydberg states: a particle in a $1/r$ potential. The difference is in the largely different reduced mass of the particle. It is useful to extend the common practice of using 'atomic units' for describing Rydberg states to ion-pair states by introducing 'molecular units', obtained by substituting the electron mass m_e in the definition of atomic units with the reduced mass of the ion-pair state, $\mu = M_A M_B/(M_A + M_B)$. Textbook formulae given in atomic units can thus be applied to ion-pair states when they are understood in these 'molecular units'. The scaling of these 'molecular units' with mass and their relation with atomic units is given in table 2, where M denotes the reduced ion-pair mass in units of the electron mass $M = \mu/m_e$. Numerical values are given for the H^+H^- system with $M = 918.5761$. Some atomic units do not involve the electron mass, like the Planck constant $\hbar$, the elementary charge e and the unit of velocity (Bohr velocity, $v_0 = a_0/\tau_0$), which remain unchanged.

All molecular or ion-pair units scale with some power of M, e.g. the Rydberg constant scales linearly, leading to a value of 1.008021×10^8 cm^{-1} for the H^+H^- system. In terms of these rescaled units the formulae for the physical behaviour, as given in table 3, remain the same. Hence the energies of the Rydberg states follow $E = -0.5n^{-2}$ and the level spacings follow $\Delta E = n^{-3}$, which can be applied to ion-pair states, when interpreted in ion-pair units. The values of these newly defined molecular units are given in SI units in the last column of table 2, for the specific case of H^+H^-.

Alternatively the physical expressions can be rewritten in SI units, transferring the mass scaling to the physical laws describing the ion-pair system. The resulting expressions for ion-pair systems in terms of SI units and in terms of the mass-scaling factor M are also listed in table 3. It is worth noticing that ion-pair states with a given principal quantum number are much more strongly bound and have a much smaller orbital radius than the corresponding Rydberg states. For small quantum numbers this leads to unphysical values for molecular energies and bond lengths, but due to the non-vanishing size of the ions this regime is never reached.

From the experimental perspective it is more instructive to compare the ion-pair system with a Rydberg electron at a given binding energy $-E$. From the Coulomb potential being exactly the same for an ion-pair and an electron bound to a singly charged ion, it follows that states bound with the same energy have the same size in both systems, but very different quantum numbers. Substituting $n = [R_\infty M/(-E)]^{1/2}$ leads to expressions for the quantities scaled to energy; the expressions and resulting values in SI units are given in table 4. Note that the mass scaling of quantities is different whether written as a function of energy or of principal quantum number. For example, the Rydberg state splitting scales with M at a given n, but with $M^{-1/2}$ at a given E.

As a result the Inglis–Teller limit scales as $1/M^{1/2}$ for an ion-pair system. Here lies the basis for an important effect in ion-pair states: their sensitivity to electric fields. Already for a light system such as H^+H^- the

Table 3. Some physical laws and expressions for Rydberg systems, in atomic units (au), their formulae for ion-pair systems including the constants (ip), and the numerical value for H^+H^-. Energies are substituted by corresponding wave numbers for ease of use in spectroscopy. In some equations $n-1$ is replaced by n, which is, at the high quantum numbers encountered, a good approximation.

Quantity	Symbol	Law (au)	Law (ip)	Value
Binding energy	$E(n)$	$-\frac{1}{2n^2}$	$-\frac{R_\infty M}{n^2}$	$-1.008021\times10^8\,\mathrm{cm}^{-1}n^{-2}$
Level spacing	$\Delta E(n)$	$\frac{1}{n^3}$	$-\frac{2R_\infty M}{n^3}$	$2.016042\times10^8\,\mathrm{cm}^{-1}n^{-3}$
Kepler radius	$R(n)$	n^2	$\frac{a_0 n^2}{M}$	$5.760842\times10^{-14}\,\mathrm{m}\,n^2$
Kepler orbit time	T_n	$2\pi n^3$	$\frac{2\pi\tau_0 n^3}{M}$	$1.654549\times10^{-19}\,\mathrm{s}\,n^3$
Stark splitting	$\delta E_s(n,F)$	$3Fn$	$\frac{6R_\infty Fn}{MF_0}$	$1.393930\times10^{-7}\,\mathrm{V}^{-1}\,Fn$
Stark osc. time	$\tau_s(n,F)$	$\frac{2\pi}{3Fn}$	$\frac{2\pi\tau_0 F_0 M}{3Fn}$	$2.392976\times10^{-4}\,\mathrm{s\,V\,cm}^{-1}\,(Fn)^{-1}$
Stark envelope	$\Delta E_s(n,F)$	$3Fn^2$	$\frac{6R_\infty Fn^2}{MF_0}$	$1.393930\times10^{-7}\,\mathrm{V}^{-1}\,Fn^2$
Inglis–Teller limit	$F_{IT}(n)$	$\frac{1}{3n^5}$	$\frac{M^2F_0}{3n^5}$	$1.446300\times10^{15}\,\mathrm{V\,cm}^{-1}\,n^{-5}$

Table 4. Some of the physical laws and expressions from table 3, written as a function of binding energy instead of principal quantum numbers, in scaled atomic units and in SI units. Energies are to be taken as wave numbers. All numerical values pertain to H^+H^-.

Quantity	Law scaled to E	Value
Level spacing	$2\left(\frac{(-E)^3}{R_\infty M}\right)^{1/2}$	$1.992027\times10^{-4}\mathrm{cm}^{1/2}\,(-E)^{3/2}$
Stark splitting	$6\frac{F}{F_0}\left(\frac{R_\infty^3}{-EM}\right)^{1/2}$	$1.399509\times10^{-3}\,\mathrm{V}^{-1}\,\mathrm{cm}^{-1/2}\,F(-E)^{-1/2}$
Stark osc. time	$\frac{2\pi\tau_0 F_0}{3F}\left(\frac{(-E)M}{R_\infty}\right)^{1/2}$	$2.383436\times10^{-8}\,\mathrm{s\,V\,cm}^{-1/2}\,F^{-1}(-E)^{1/2}$
Stark envelope	$6\frac{F}{F_0}\frac{R_\infty^2}{-E}$	$1.405111\times10^{1}\,\mathrm{V}^{-1}\,\mathrm{cm}^{-1}\,F(-E)^{-1}$
Inglis–Teller limit	$\frac{F_0}{3}\left(\frac{(-E)^5}{R_\infty^5 M}\right)^{1/2}$	$1.417701\times10^{-5}\,\mathrm{V\,cm}^{3/2}\,(-E)^{5/2}$

Inglis–Teller limit is at field strengths thirty times smaller than in atomic Rydberg systems, for the same binding energy $-E$. The sensitivity of high-n Rydberg states to stray fields and the presence of ions is strongly amplified [39].

2.4. *Stark effect in a heavy Rydberg system*

The Schrödinger equation for an electron in a combined Coulomb and homogeneous electric field, represented by the Hamiltonian

$$H=-\frac{\hbar^2}{2\mu}\nabla^2-\frac{e^2}{4\pi\epsilon_0 r}+eFz \tag{6}$$

can be solved analytically in parabolic coordinates, leading to the linear Stark effect for the hydrogen atom, with field-independent wave functions, in the weak-field limit. Energies of these states are given in first order by [40]

$$E=-\frac{R_\infty}{n^2}+3R_\infty\frac{F}{F_0}n(k_1-k_2), \tag{7}$$

with n the principal quantum number, and k_1 and k_2 the parabolic quantum numbers, where k_1 goes from 0 to $n-1$ and $k_2 = n - k_1 - 1$. For the numerical evaluation of equation (7) the values for the Rydberg constant and the electric field have to be taken in the mass-scaled units for the H^+H^- system. The second-order contribution to the Stark effect, giving rise to further splitting of the k-levels in magnetic substates m via [39]

$$E^{(2)} = -\frac{R_\infty}{8}\left(\frac{F}{F_0}\right)^2 n^4\left[17n^2 - 3(k_1 - k_2)^2 - 9m^2 + 19\right], \tag{8}$$

is not taken into consideration.

In figure 3 a plot is made of the Stark levels as a function of electric field strength F using equation (7). Note that in the figure only the lowest and highest Stark sub-level for each value of the principal quantum number n is represented. Also shown in the figure are those states that are energetically allowed to contribute to the wave packet when an H^+H^- state is formed at $13.7\,\mathrm{cm}^{-1}$ binding energy at a field of $1.4\,\mathrm{V\,cm}^{-1}$, with a laser pulse of a certain bandwidth (150 MHz). Stark states belonging to more than 100 different principal quantum numbers are present. Figure 4 shows the Stark manifold at this energy and field strength in detail, with a (somewhat arbitrary) field range of $5\,\mathrm{mV\,cm}^{-1}$ to give an impression of the local variation between individual H^+H^- systems inside the interaction region if the field is not exactly homogeneous. In figure 4 all levels pertaining to all quantum numbers n, k_1 and k_2 are plotted. It is obvious that the exact composition of such a wave packet is very sensitive to slight differences in the electric field, accordingly all measurements represent an ensemble averaging. However, the dynamical properties of the H^+H^- system depend much less on the field strength than the details of the level structure do.

2.5. *Saddle point lowering and field dissociation*

In an electronic Rydberg system, the presence of an electric field leads to ionization when the excitation energy exceeds the energy of the saddle point which is

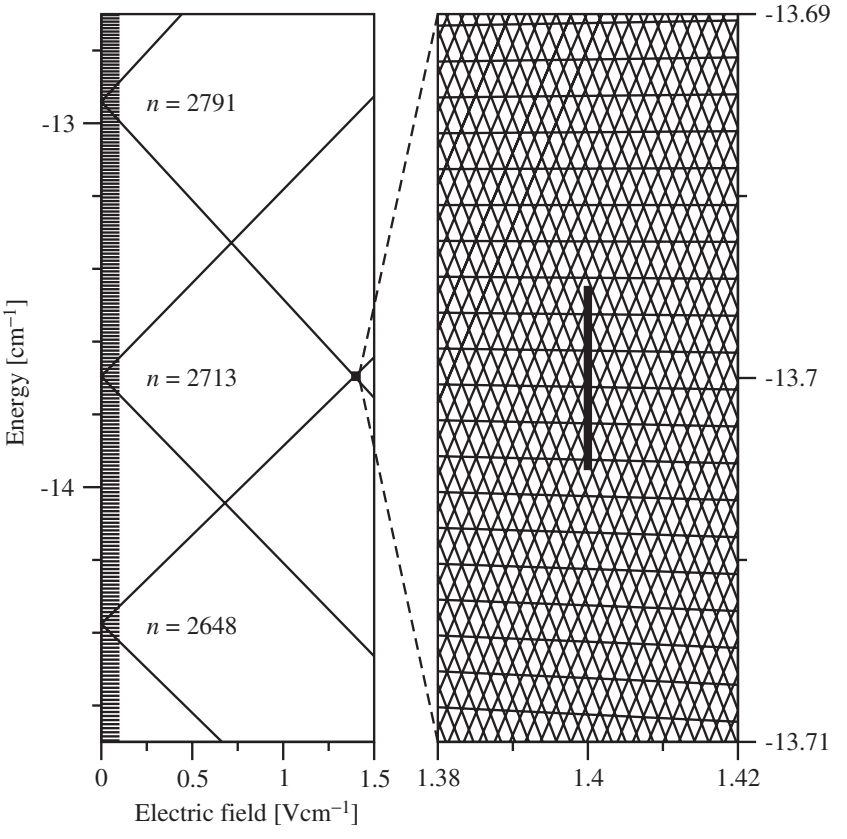

Figure 3. Part of the Stark state manifold of the H^+H^- system involved in excitation at $-13.7\,\mathrm{cm}^{-1}$ and $1.4\,\mathrm{V\,cm}^{-1}$. Only the central and the outermost states of principal quantum number and their Stark systems are displayed. The blow-up shows the parameter range for the ensemble of molecules in one measurement, while the central section represents the coherent superposition of states in the wave packet in one molecule.

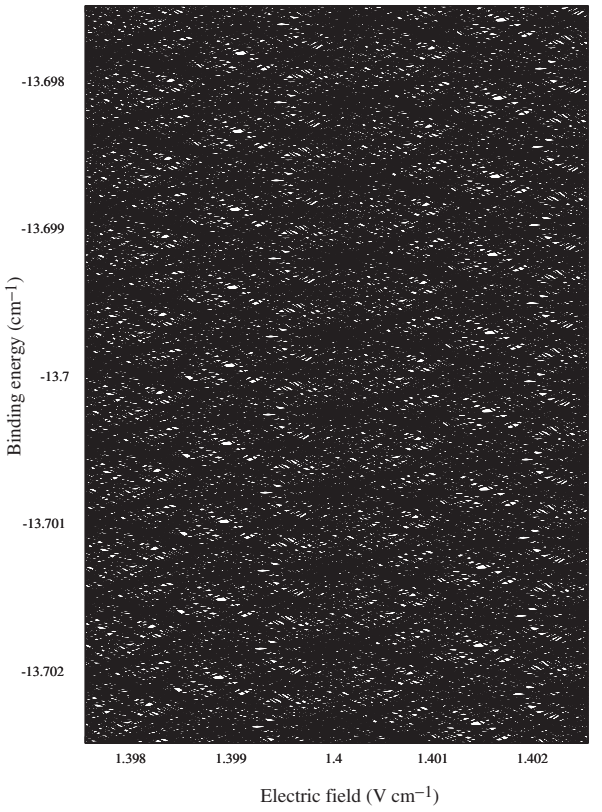

Figure 4. Plot of all Stark levels for the conditions of figure 3. Considerable change in the details of the level structure is visible even for sub-mV cm^{-1} field variations. At any given field strength within the interaction zone, all displayed levels are coherently excited with a laser pulse of 150 MHz bandwidth.

formed in the combined Coulomb potential and the linear external potential. The same occurs in a heavy ion-pair system, although the process might more appropriately be called 'field dissociation' [8]. The binding energy, down to which field dissociation occurs as a function of the field strength, depends on whether the field is already present during excitation or not, and in the latter case also on dynamics of the time evolution of Rydberg states into Stark states. In any case the lowering of the dissociation threshold as a function of the field scales as $\Delta E \propto F^{1/2}$, but the proportionality factor differs. For a temporally constant field, it is identical to the saddle point lowering in the potential, which is $\Delta E = 6.12\,\mathrm{cm}^{-1}/(\mathrm{V\,cm}^{-1})^{1/2}\,F^{1/2}$. When the field increases slowly so that the Rydberg states evolve into the Stark states, the factor is only $4\,\mathrm{cm}^{-1}/(\mathrm{V\,cm}^{-1})^{1/2}$ [4] if the evolution through the crossings with Stark manifolds of different principal quantum numbers is diabatic; if the crossings are really avoided crossings and the evolution is adiabatic, the factor is again $6\,\mathrm{cm}^{-1}/(\mathrm{V\,cm}^{-1})^{1/2}$.

2.6. *Quantum defects*

Ion-pair states with small principal quantum numbers, thus having bond lengths of the order of the scaled Bohr radius, are unphysical because the ions themselves are orders of magnitude larger. In the H^+H^- case the proton penetrates the H^- wave function at a separation of $R \approx 2 \times 10^{-10}$ m ($\langle r^2 \rangle$ value of the electron density 11.9 a_0 [38]). Therefore the principal quantum numbers of the lowest possible ion-pair states are formally given by $R = n^2 a_{0\mathrm{eff}} > 2 \times 10^{-10}$ m, i.e. $n > 60$, or put another way, the quantum defect is $\delta > 60$. At this internuclear distance the ion-pair configuration becomes discernible in several Born–Oppenheimer potentials of the H_2 molecule: in the $\bar{H}^1\Sigma_g^+$ and the $\bar{B}^1\Sigma_u^+$ potentials; then again 4000 cm^{-1} lower, below the avoided crossings with the states at the H(1s)+H(2ℓ) threshold, in the outer well in the $EF^1\Sigma_g^+$ potential and the broad outer slope in the $B^1\Sigma_u^+$ potential. Calculations show that even the $X^1\Sigma_g^+$ ground state of H_2 has an in-pair contribution to its wave function. None of them is just 'the' ion-pair potential at short internuclear separation, making the numbering of low ion-pair quantum states, and thus the integer part of the quantum defect, rather arbitrary. As a consequence, a quantum defect treatment of the H^+H^- configuration cannot be singled out from a combined multichannel quantum defect description of the manifold of channels with which the ion-pair channel strongly interacts.

3. Experimental set-up

In the experiment two-step photo-excitation is combined with field dissociation either by DC or pulsed electric fields. In a first laser excitation step, induced by a tunable extreme ultraviolet (XUV) nanosecond pulsed laser source based on third harmonic generation in a pulsed gas jet, single rovibrational quantum states in H_2 are prepared: $B^1\Sigma_u^+$, v, $J = 0$ and $J = 2$ in ortho-hydrogen and $J = 1$ in para-hydrogen. Alternatively also $C^1\Pi_u$ states have been used as intermediates, but signal strengths are generally much weaker and thereby insufficient. Subsequently the H_2 molecules are further excited by a narrowband (150 MHz) pulsed UV laser tuneable in the range 310–330 nm to reach the H^+H^- ion-pair limit at 139 714 cm^{-1} above the ground state. The pulse duration of this nearly Fourier-transform limited laser is $\approx$5 ns. Several aspects of the narrowband XUV-laser source and its use in conjunction with additional lasers and in application to the study of molecular hydrogen have been described in [26]. One important issue for the present laser excitation scheme is the use of a geometric separation of the generated XUV beam from the fundamental UV beam [41].

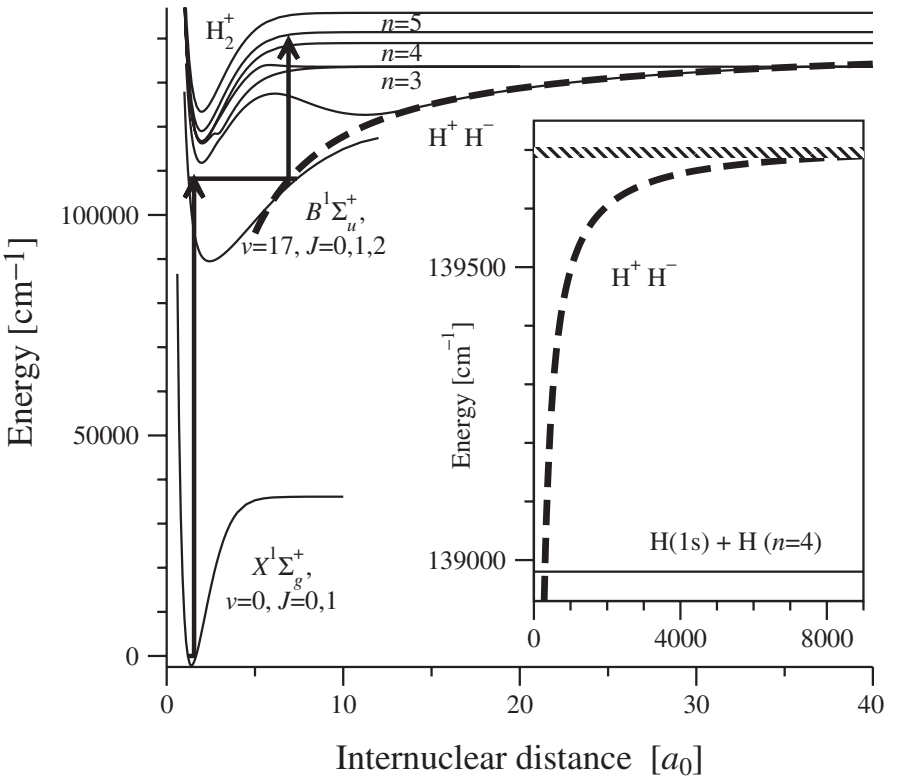

Figure 5. Potential curves of H_2, showing the pathway of two-step excitation of the H^+H^- system interacting with Rydberg states at small internuclear distance. The inset shows the H^+H^- potential on a larger scale together with the fourth dissociation threshold of H_2; the shaded region indicates observed bound ion-pair states.

In figure 5 the laser excitation scheme is plotted with reference to the relevant potential energy curves of H_2. In the interaction zone, the two laser beams, which are counter-propagating and temporally overlapped, a homogeneous DC field of several V cm^{-1} as well as a pulsed electric field of up to 50 V cm^{-1} can be applied. Ions produced by the combination of laser excitation and electric fields propagate through a mesh towards a field-free time-of-flight mass separator, at the end of which an electron multiplier is mounted for ion detection. Both H^+, H_2^+ and, via opposite poling of the fields, also H^- ions can be collected. Also the option of orienting the DC and pulsed fields parallel or anti-parallel is available. More details are given in the caption of figure 6 showing the geometry of the interaction region and the pulse sequences.

Four different types of experiments are performed. First, the region near the H^+H^- limit is scanned, below and above the limit, in the presence of a constant electric field. In this case either the prompt H^+ or H^- are detected, that are produced above the H^+H^- limit, which is slightly shifted by the applied DC field. Such a scheme was previously explored by Pratt *et al*. [8].

Secondly, excitation is performed in a small (0.1–3 V cm^{-1}) constant field F_1, while a pulsed electric field F_2 is switched on, parallel or anti-parallel to the DC-field, after a certain constant delay of up to 2 μs. This is the typical scheme of threshold ion-pair production spectroscopy (TIPPS) as first used by the group of Hepburn [9, 12], but now after two-step laser excitation. In both these experiments the second laser is scanned and spectral features are observed.

In the third type of experiment, oscillating Stark wave packets are detected, with the two lasers kept fixed in wavelength probing a small part ($\Delta\nu = 150$ MHz) of the energy region at 8–25 cm^{-1} below the H^+H^- limit. Excitation is again performed in a small DC field, while a pulsed field is applied, for which the delay with respect to the laser pulses is scanned between 0 and 2 μs. Both parallel and anti-parallel DC–AC field configurations are used giving different outcomes to be discussed in this paper. Furthermore an important characteristic of the pulsed field is its rise time, which is relatively slow compared to the duration of the laser pulses and the dynamical evolution of the wave packets to be probed; this characteristic and its implications will be discussed.

In a fourth set of experiments a third pulsed laser at various near-infrared wavelengths is used. For this

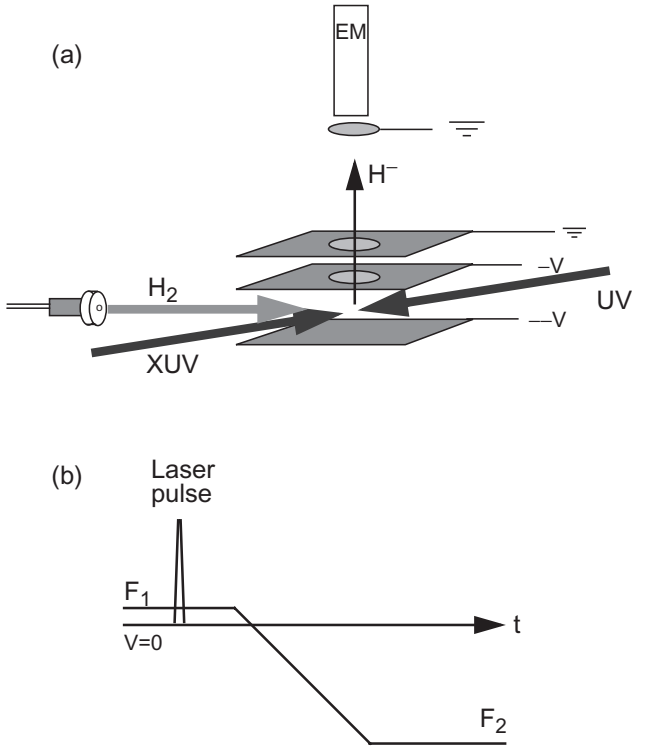

Figure 6. Layout of the set-up inside the vacuum chamber in which the heavy Rydberg states are prepared and probed in the various schemes described in the text. (a) A pulsed beam of H_2 is produced by a pulsed valve and collimated by a skimmer to enter the interaction region where it is crossed by the temporally and spatially overlapped counter-propagating laser beams. DC and pulsed voltages are put on capacitor plates, combined with a third grounded plate to satisfy Wiley–McLaren space focusing conditions. In the specific experiment where heavy Rydberg wave packets are probed a time sequence as displayed in (b) is adopted. The drawn scheme applies to the case of anti-parallel fields, where optical excitation takes place in a small DC field F_1, given by the DC value of ('–V'– '––V')/25 mm. Production and extraction of H^- is established by the anti-parallel field pulse F_2 that directs ions into the time-of-flight drift tube (15 cm length) and further onto the electron multiplier (EM) detector. Note that the rise time of the pulsed field F_2 is on the order of several μs, which is slow compared to the time scale of observed dynamics.

purpose a simple optical parametric oscillator (OPO) was built, with a compact and linear configuration and a β-barium borate (BBO) nonlinear crystal pumped at 355 nm. Stepwise tunable near-infrared pulses were produced close to 1600 nm at fairly large bandwidth ($\Delta\lambda = 2$ nm). These pulses were applied at a certain fixed delay ($\approx$150 ns) after the two initial XUV and UV pulses, probing bound ion-pair states. The third near-IR laser clearly induces a H^+ signal, particularly above the threshold, when the wavelength becomes shorter than 1459 nm. Hence in this experiment the near-IR laser excites $H(n = 4)$ fragments to the ionization continuum. Thus it provides proof for the decay of heavy Rydberg states into neutral fragments with a significant channel producing $H(n = 1) + H(n = 4)$. A comparable phenomenon of a strong dissociation onset was found at the $n = 3$ dissociation threshold [42].

4. Time-domain observations and models

4.1. *Oscillating Stark wave packets*

In this section the observations on the oscillatory behaviour in the pulsed-field delay scans are presented. During these measurements two-step laser excitation is applied in a small DC electric field, and H^+ or H^- ions are detected; the ions are produced by pulsed field dissociation after a certain temporal delay, which is scanned in repetitive measurement sequences. Results of six typical time delay scans, obtained at various settings for the binding energy probed by the laser, and for the DC electric field, are presented in figure 7. The crucial observation in this work is the oscillatory behaviour superimposed on the decay transients, which are representative for the lifetime of the Rydberg states. The data in figure 7 are taken with a configuration of anti-parallel directions of the DC and the pulsed electric fields.

A central observation in these recurrence spectra is that all oscillations match the Stark oscillation time, which can be calculated to equal (see also table 3)

$$\tau_s(F) = \frac{h}{\delta E_s} = 2.383 \times 10^{-8}\ \mathrm{s}\ \frac{(-E/\mathrm{cm}^{-1})^{1/2}}{F/(\mathrm{V\,cm}^{-1})} \qquad (9)$$

for various conditions of binding energies and electric fields.

The detailed shape of the ion signal as a function of pulse delay is not obvious from the physics of the wave packets and their decay. H^+ and H^- ions must originate from surviving H^+H^- systems at the time of the electric field pulse, because their formation through prior decay is energetically excluded. But the yield is not necessarily proportional to the population. Otherwise one would not observe minima in the yield as a function of time, as clearly visible in figure 7.

Ion formation in the detection scheme is a complex process, because the rise time of the electric field is not short compared to the dynamic time scales in the molecule. Typically the field only reaches the strength at which H^+ and H^- are dissociated after several 100 ns; we note again that the slow rise time of the pulsed field is a characteristic of our set-up. During this time, the Stark state splitting changes according to the changing electric field. Details of the resulting change in the dynamics of the H^+H^- wave packet may be modified by the

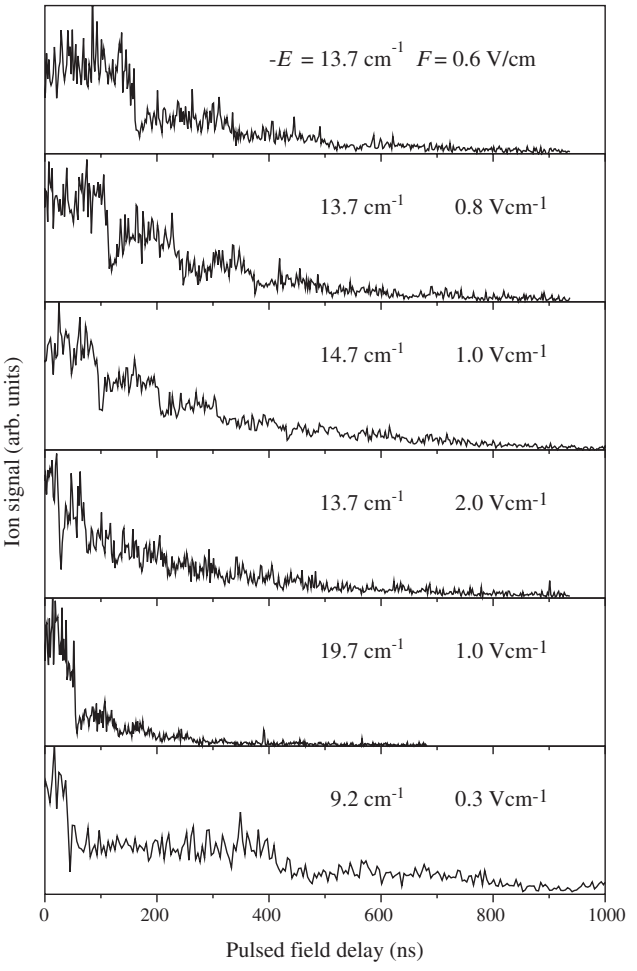

Figure 7. A set of recurrence spectra recorded at various binding energies and DC electric field strengths as indicated.

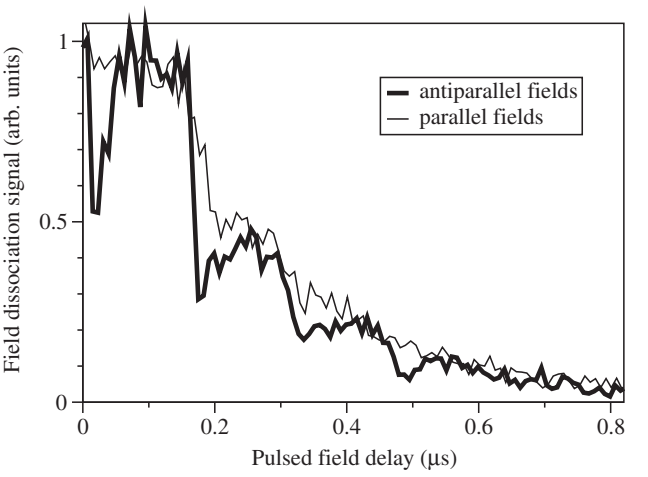

Figure 8. Field dissociation signal from H^+H^- as a function of pulsed field delay, with the DC field oriented either parallel or anti-parallel to the pulsed field. Both measurements were done at a binding energy of $13.7\,cm^{-1}$ and a DC field of $0.6\,V\,cm^{-1}$.

quadratic Stark effect, and a non-adiabatic evolution of the Stark state occupation with the varying field. It is however a safe assumption that the dynamics during the detection field pulse is identical for any two points on a delay spectrum that are separated by one oscillation period of the H^+H^- system in the DC field, because the wave packet prior to the field pulse is identical except for the decreasing population. Periodic, narrow minima in figure 7 indicate that there exists a small time window for each wave packet cycle in which the ion production probability by the detection field is strongly reduced. Figure 8 shows that these minima only occur when the DC field and the detection field have opposite orientation, which can be explained as follows.

The angular momentum of the molecule is not a conserved quantity in the presence of external fields, but nevertheless angular momentum selection rules determine the population of the initial wave packet: the intermediate state, the B state, is almost unaffected by the small field and therefore in a well-defined angular momentum state with low quantum number. Dipole selection rules $\Delta J = 0, \pm 1$ imply that the B state only couples to up to three low-J components in the ion-pair state; actually only $\Delta J = \pm 1$ is allowed because both states are Σ^+ states, which do not have substates of inverse electronic parity and therefore require a parity change in the rotational part of the molecular state. While selection rules are valid in the absence of an external field, parabolic wave functions are eigenstates of the Hamiltonian at any field strength down to zero in the case of the linear Stark effect. Transformation into the basis of parabolic wave functions shows that the low-J excited state at zero field is a coherent superposition of a large number of Stark states. The situation remains unaltered when a wave packet is excited by a short pulse in a small electric field, as long as the Stark state splitting is indiscernible within the excitation time in terms of energy–time uncertainty. Therefore the initial wave packet must be a superposition of a few low-J components, allowed by selection rules for zero field, in a very good approximation. The angular momentum then changes with time due to the electric field, but the spread of J remains small because the splitting between Stark states is almost equal.

In the anti-parallel field configuration, the total field during the pulsed field rise time initially decreases to zero, slowing down the evolution of the H^+H^- wave packet and leaving it in a superposition of states with well-defined angular momentum quantum numbers for a short time. If the wave packet happens to be in states with low J in this time interval, H^+ and H^- have a

strong wave function overlap, and therefore there is a high probability of the H^+H^- system decaying by molecular autoionization or neutral fragmentation. If the wave packet is in higher J states, the H^+H^- system survives the time interval of almost zero electric field, and has a much lower probability of decaying prior to field dissociation into H^+ and H^-. The sharpness of the minima indicates that the spread of the wave packet in angular momentum remains small, and that the fraction of angular momentum states contributing to decay through non-adiabatic molecular processes is small as well; the latter is consistent with the conclusions drawn below from the observed H^+H^- lifetimes as discussed in section 4.4. The minima gradually smear out after more oscillation periods, indicating an increasing spread in angular momentum space due to slightly different linear Stark coefficients of the states with different principal quantum numbers present in the wave packet. In comparison, the effect of the quadratic Stark effect is negligible at the given field strengths, and so are apparently the effects due to field inhomogeneities.

4.2. *Oscillation frequencies*

Figure 9 shows the observed oscillation frequencies, given by $1/T_r$ as a function of $F/(-E)^{1/2}$. For the entire range of energies and field strengths investigated, including measurements of para- and ortho-hydrogen and excitation via different rotational levels of the intermediate B state, the results fit to a single straight line. Next to the linear fit, figure 9 also displays the oscillation frequencies predicted from equation (9):

$$f = 41.96\,\mathrm{MHz}\frac{F/(\mathrm{V\,cm^{-1}})}{(-E/\mathrm{cm^{-1}})^{1/2}}. \qquad (10)$$

The agreement between theory and experiment is good but not perfect; the experimental slope is $(39.94 \pm 0.45)\,\mathrm{MHz\,(V\,cm^{-1})^{-1}\,(cm^{-1})^{1/2}}$, and there is a small but significant non-zero offset of $(1.14 \pm 0.15)\,\mathrm{MHz}$ as well. Theoretical values fall outside the statistical 3σ uncertainties of the linear fit parameters.

The origin of this discrepancy is not well understood, especially, whether it is an experimental artefact or a real feature of the H^+H^- system. On the one hand, systematic errors in the determination of binding energies as well as the DC field would have to be on average $2\,\mathrm{cm^{-1}}$ and $0.3\,\mathrm{V\,cm^{-1}}$, respectively, to make the data fit theory. Such a large error of the binding energy $-E$ can be excluded with high confidence. However, in the determination of the electric field F, assumed to be the DC voltage on the capacitor divided by the plate distance of 25 mm, a systematic error of the required magnitude is possible. Figure 8 shows oscillation frequencies with DC fields on both orientations with identical external voltage on the capacitor; upon close inspection, one notices a discrepancy in oscillation frequencies, which would correspond to a field difference of $0.16\,\mathrm{V\,cm^{-1}}$. The exact origin of the field offset is unknown, but such fields can easily arise from contact potentials between e.g. the metal of the field plates and impurities on their surfaces. An average field offset of $\approx 0.3\,\mathrm{V\,cm^{-1}}$ would explain the offset of the linear fit in figure 9, but not the deviation of the slope from theory.

On the other hand, the discrepancy from the prediction of the linear Stark model is not removed either by including the quadratic contribution to the Stark effect for a hydrogenic system, scaled appropriately with the large mass, which changes level spacings by only about 1%. An important deviation from a hydrogenic Rydberg system however is the presence of an extended H^- 'core'. From the size of the H^- wave function and orbital parameters of the H^+H^- Rydberg states one can estimate that states with about $J \leq 60$ are core penetrating; this is discussed in more detail in connection with decay in section 4.4. This small fraction of the wave function components in Stark states with $n = 2000$–3500 should influence the dynamics by about 2–3% of the evolution period, consistent with the sharpness of observed minima in the oscillations ascribed to core effects. In comparison, the deviation of the empirical from the theoretical slope corresponds to a discrepancy of 10–20% of the evolution time.

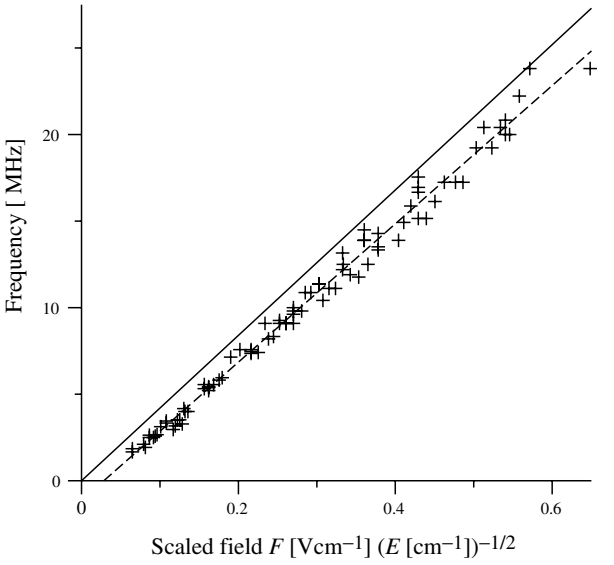

Figure 9. Observed oscillation frequency of the observed recurrences as a function of the scaled field strength $F/(-E)^{1/2}$. The solid line is the theoretical function based on the linear Stark model, the dashed line shows a linear fit of experimental data. Data pertain to para- as well as ortho-hydrogen.

To settle this problem, better control of stray electric fields in the experimental environment is required, while magnetic fields may also be an issue.

4.3. *Model for wave-packet decay*

In the two-photon excitation process a coherent wave packet is excited, at time $t = 0$ and the wave packet is denoted as $\Psi(0)$. The initial wave function $\Psi(0)$ comprises a large number of heavy Rydberg states as shown in figure 4, but also an admixture of predissociating and autoionizing short-range states, which presumably also provide the oscillator strength for excitation. The time-dependent decay rate is proportional to the absolute square of the projection of the wave packet on its initial state, with an additional factor γ_t reflecting the decay rate of the initial state and other similar short-range states contributing to the decay. If the initial composition of the wave packet is given by $\Psi(0) = \sum_i c_i \psi_i(0)$, and the time evolution of Stark states ψ_i by $\psi_i(t) = \psi_i(0) \exp(\mathrm{i}E_i t/\hbar)$, the time-dependent projection of the wave packet on its initial state is

$$\langle \Psi(0)|\Psi(t)\rangle = \sum_{i,j} c_i^* c_j \exp\left(\frac{\mathrm{i}}{\hbar} E_j t\right)\langle \psi_i|\psi_j\rangle = \sum_i |c_i|^2 \exp\left(\frac{\mathrm{i}}{\hbar} E_i t\right), \tag{11}$$

the latter because the Stark states are orthonormal. In the summation over i and j only the heavy Rydberg states are included, while the experimental decay is considered to be a consequence of coupling to dissociative and ionization continua.

The time dependence can be derived from the state density function of the wave packet, i.e. the density-of-states distribution weighted by the corresponding absolute squares of the superposition coefficients of the wave packet $\tilde{f}(E) = \sum_i |c_i|^2 \delta(E_i)$ (the contribution of individual states is idealized by the Dirac δ distribution). Written in terms of frequencies the density function is $\tilde{f}(\omega) = \sum_i |c_i|^2 \delta(\omega_i)$, with $\omega_i = E_i/\hbar$ and $\delta(\omega_i) = \hbar\,\delta(E_i)$. Now the (inverse) Fourier transform leads to

$$f(t) = \int_{-\infty}^{\infty} \tilde{f}(\omega) \exp(\mathrm{i}\omega t)\,\mathrm{d}\omega = \sum_i |c_i|^2 \int_{-\infty}^{\infty} \delta(\omega_i) \exp(\mathrm{i}\omega t)\,\mathrm{d}\omega = \sum_i |c_i|^2 \exp\left(\frac{\mathrm{i}}{\hbar} E_i t\right), \tag{12}$$

which equals equation (11). Unfortunately the initial superposition coefficients c_i are not known, but the constraint of the optical selection rules dictates that the states have a well-defined, small angular momentum. The presence of a given angular momentum state in all Stark states, with small superposition coefficients, causes all Stark states within the excitation energy width to contribute to some extent. As a simplification we therefore assume all $|c_i|^2$ to be equal, in which case $\langle \Psi(0)|\Psi(t)\rangle$ equals the Fourier transformed density of states function in the energy interval that is covered by the spectral width of the excitation pulse, see figure 4.

While the complex Fourier-transform of the state density depends as strongly on the electric field strength as does the exact state distribution, it is mainly the complex phase that changes, where the absolute values change much slower. Thus the time-dependent decay rate, which is proportional to $|f(t)|^2$, is essentially identical over a field range larger than shown in figure 4. The population as a function of time, $p(t)$, then becomes

$$p(t) = p(0) \exp\left(-\int_0^t \gamma_t |f(\tau)^2|\,\mathrm{d}\tau\right). \tag{13}$$

Figure 10 shows the resulting function $p(t)$ together with an experimental signal, taken under identical conditions of a binding energy of $-13.7\,\mathrm{cm}^{-1}$ and a field of $1.4\,\mathrm{V\,cm}^{-1}$.

The model calculation matches a number of features of the experimental observation: initially the population decreases in sharp steps, but later on the steps wash out

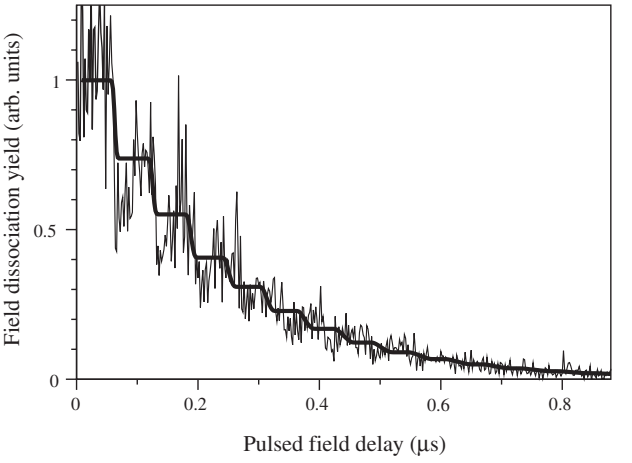

Figure 10. Modelled stepwise decay of the H^+H^- population at a binding energy of $13.7\,\mathrm{cm}^{-1}$ in a field of $1.4\,\mathrm{V\,cm}^{-1}$. Superimposed is an experimental pulsed field dissociation signal measured in the same conditions. The observed lifetime is 210 ns, corresponding to 42 low-J decay channels with a 100% decay efficiency at core penetration, happening once per Kepler orbit time of 3.302 ns.

such that after more than ten steps, the remaining decay is more or less exponential. This even occurs at a fixed value of the field, and is therefore not associated with the inevitable ensemble averaging over molecules in residual stray fields. The oscillation period in the simulation differs slightly from the observed one, which is reflected by the fact that observed values do not lie on the solid line in figure 9. Obviously the step distance in the simulated curve reflects the level splitting of the linear Stark model.

4.4. *Lifetimes of heavy Rydberg states*

Lifetimes of Rydberg states are usually determined by decay near the core, leading to an n^3 dependence, whether the dominant process is fluorescence or some inelastic core scattering effect. This holds for states with well-defined angular momentum, for which the wave function density at the core decreases with n^{-3} without much further change at high n. Stark states in sufficiently strong fields, or at any field strength in the case of the linear Stark effect, however are superpositions of angular momentum components spanning the entire range $0 \leq J < n$. As the higher-J components are non-core-penetrating states, this leads to an enhanced lifetime scaling with n^4. Also when the electric field direction changes rapidly, the projection of J may not be conserved, and the mixing of m components may even lead to an increase by n^5. This is observed when ions are present or close encounters between Rydberg systems are probable [43].

The observed stepwise decay reflects the time-dependent population of angular momentum states, but over time scales that are long compared to the wave packet dynamics, the population decreases more or less exponentially with a time constant that reflects the time-averaged population of J states, with empirical time constants shown in figure 11. Unfortunately, in many measurements there are only a few oscillation cycles, leading to a large uncertainty in the respective time constant. A linear fit of the double-logarithmic plot lifetime versus binding energy gives a slope of -1.97 ± 0.14 or equivalently $\tau \propto n^{3.94\pm0.28}$, which is consistent with the expected n^4 dependence. Taking this fixed value in the exponent, the fitted value of the intercept becomes $\ln(\tau/\mathrm{ns}) = 10.93 \pm 0.35$ at $\ln(E/\mathrm{cm}^{-1}) = 0$. The final result for the lifetime of H^+H^- in an electric field with n between 2000 and 3500 is then (with a slight adjustment to get a symmetric uncertainty interval)

$$\begin{aligned}\tau &= (5.8 \pm 2.0) \times 10^{-21}\,\mathrm{s}\,n^4 \\ &= (5.9 \pm 2.0) \times 10^{-5}\,\mathrm{s}\,(\mathrm{cm}^{-1}/E)^2. \end{aligned} \quad (14)$$

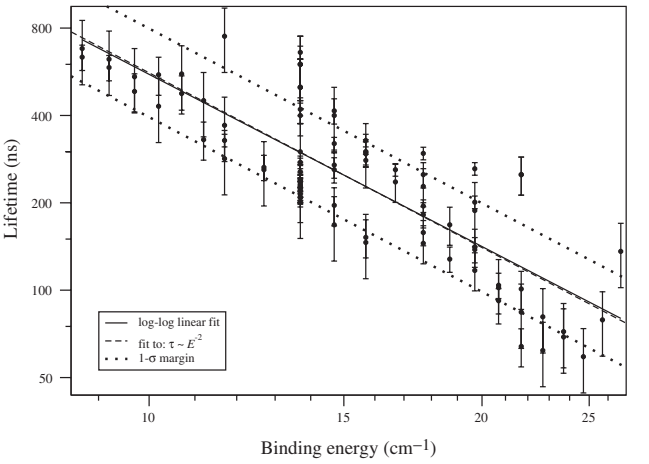

Figure 11. Lifetimes of H^+H^- states as a function of binding energy, obtained from fitting an exponential to the decay transients. States in various electric fields are included in the same graph. The solid line represents a linear fit to all data on a double-logarithmic scale, the dotted line gives shows a fit based on $\tau \propto n^4 \propto E^{-2}$ and the margin of one standard deviation of experimental values.

From this result the effective number of low angular momentum channels that contribute to the decay can be determined. With the semi-classical assumption that the shortest possible lifetime of a core-penetrating state is its Kepler orbit time, given by $T = 2\pi n^3$ in atomic units, which equals $T = 1.6545 \times 10^{-19}\mathrm{s}\,n^3$ for H^+H^-, the average probability that H^+H^- with lifetime τ is in such a decaying angular-momentum state is then $T/\tau = (32 \pm 10)/n$ (again with an adjusted central value to get a symmetric uncertainty interval), implying that 32 ± 10 out of the n angular momentum channels decay upon core penetration. Alternatively, more J channels may contribute, accordingly with a lower decay probability per channel.

4.5. *Decay channels for H^+H^- Rydberg states*

In order to refine the statement in the previous section on the number of angular momentum components contributing to H^+H^- decay, we consider the different autoionization and predissociation channels and the related potential curves. The contribution of these processes is strongly influenced by the change of potential shapes due to the centrifugal term $J(J+1)/(\mu R^2)$. This is very different from optically excited states that autoionize and predissociate by the same mechanisms, like the superexcited H_2 states which lead to initial formation of the ion-pair state, where the centrifugal term has only a minor effect because J is small due to optical selection rules.

Figure 12 shows the $^1\Sigma_g^+$ potentials of H_2 including the centrifugal term for different J values, which are

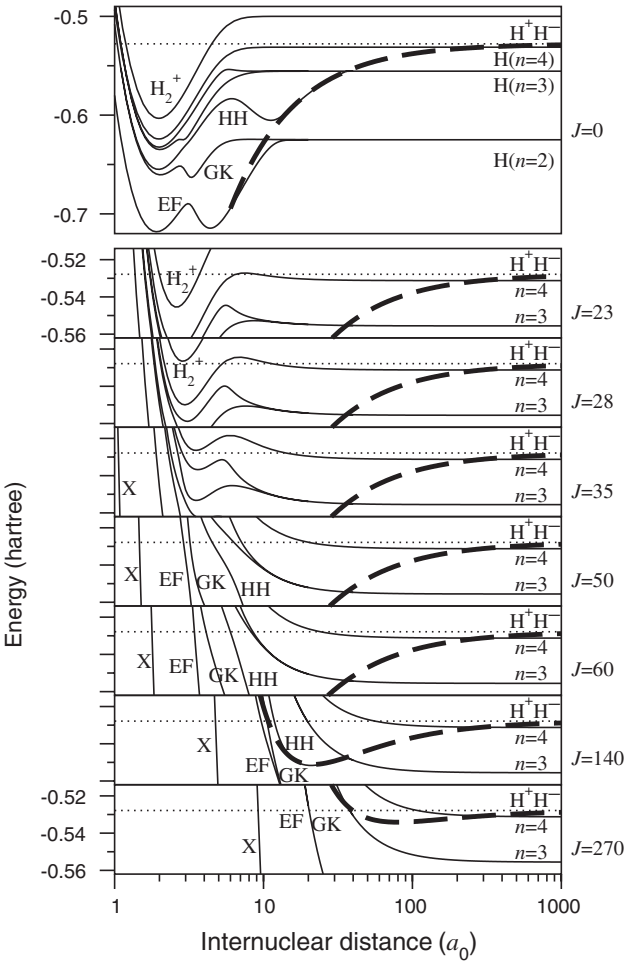

Figure 12. Upper part: $^1\Sigma_g^+$ potential manifold of H_2. The dashed line shows a fictitious unperturbed ion-pair potential, the dotted line indicates the asymptotic H^+H^- energy. R scale is logarithmic to display features at small and big R simultaneously. Lower part: potentials including the centrifugal term for various J, starting at which certain processes are suppressed. $J \geq 23$: dissociation in $n = 4$ inhibited by centrifugal barrier $J \geq 28$: autoionization energetically forbidden $J \geq 35, 50, 60$: no short-range $H(n = 4, 3, 2)$ formation $J \geq 140$, 270: no long-range $H(n = 2, 3)$ formation.

the upper limits for reaching the core regions that are relevant for a number of decay mechanisms. Similar considerations hold for decay processes through the $^1\Sigma_u^+$ manifold; they equally contribute to H^+H^- decay because the g–u symmetry is completely broken in an electric field, in the same way as electronic Rydberg states with even and odd ℓ are mixed in Stark states.

Formation of $H(n = 4)$ dissociation fragments is a strong process after optical excitation at energies directly above threshold up to the H^+H^- asymptote region, as proven by excitation with an additional IR pulse; however, it is suppressed as a decay process for H^+H^- by a centrifugal barrier in the dissociative potential for all but the lowest 23 angular momentum channels. It turns out that this is the only case in which a centrifugal barrier appears in the dissociative potential, in all others the accessible region smoothly moves outwards, while the energy of the active region is shifted above the H^+H^- asymptote. Autoionization becomes impossible next at $J \geq 28$, then at $J = 35$, 50 and 60 the various short-range predissociation processes follow.

All these decay processes involve an interaction of molecular Rydberg states with the lowest doubly-excited $(2p\sigma)^2\,^1\Sigma_g^+$ state, and they are all known to be strong in the singlet-g manifold, but weak in the u manifold where such a low doubly-excited state does not exist. One of many manifestations of this difference is the extreme broadening of otherwise long-lived $\bar{H}$ states close to the barrier in the $H\bar{H}\,^1\Sigma_g^+$ potential, where they can reach short internuclear distance [26, 44]; while comparable states close to the barrier in the $B''\bar{B}\,^1\Sigma_u^+$ potential are as long-lived as lower vibrational states [27]. From dissociative recombination studies it is known as well that the dominant coupling mechanism of the $H_2^+ + e^-$ continuum and neutral molecular states involves the unique low-lying $(2p\sigma)^2$ state [45–47]. From exchange rules for the identical nuclei it follows that in any angular momentum superposition in H^+H^-, all states with even J are of the same g–u symmetry type, while the odd J components are of the other one; unless there is mixing of 'para' and 'ortho' states, for which there is no mechanism in the H^+H^- configuration of hydrogen, with or without an electric field. Therefore the number of J channels providing strong autoionization or short-range predissociation is effectively half of the above values.

The longer-range predissociation regions, formed by avoided crossings between the H^+H^- potential and the neutral asymptotes, exist for both g and u manifolds; non-adiabatic coupling leads to Landau–Zener transitions between the potentials. They become suppressed at considerably larger angular momentum: at $J = 140$, the region becomes inaccessible where the ion-pair-like $\bar{H}\,^1\Sigma_g^+$ and $\bar{B}\,^1\Sigma_u^+$ states interact with the states correlating with $n = 2$ dissociation (EF and $GK\,^1\Sigma_g^+$, and B and $B'\,^1\Sigma_u^+$); the same happens for $n = 3$ dissociation at $J = 270$. Even if the intrinsic probability of these processes is smaller than for short-range predissociation, their overall contribution to decay of the H^+H^- system may be considerable, if not dominant; only long-range $n = 4$ dissociation, energetically allowed up to $J = 730$, can be neglected due to vanishing Landau–Zener transition probability at this potential crossing. Note the reversed order of cut-off for J values due to the location of the active region in energy and internuclear distance.

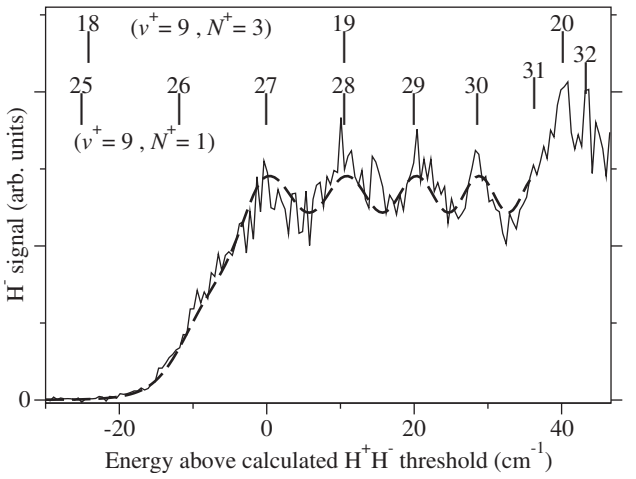

Figure 13. Threshold ion-pair spectrum of H_2, excited via the B–X(17,0)R(1) transition without external electric field. The below-threshold signal originates from bound H^+H^- states dissociated by a delayed extraction field. The excitation efficiency shows structure from electronic Rydberg series with the indicated H_2^+ core states and principal quantum numbers.

5. Frequency-domain observations and models

5.1. *Field-free near-threshold excitation*

The starting point in our investigation of the threshold behaviour near the H^+H^- limit is the field-free excitation ($F_1 = 0$) of this energetic region. In figure 13 a recording of the energy-dependent H^+H^- excitation is displayed. In this case two-photon excitation via a resonant intermediate is used; the threshold excitation depends on the specific intermediate state chosen. In this experiment the population of the excited state is probed by a switched field of $F_2 = 24\,\mathrm{V\,cm^{-1}}$, delayed by 1 μs. Such a field is sufficiently strong to dissociate with near 100% efficiency in the entire range where the H^+H^- population is observed. The signal shown is the H^- yield, which is free of background from other processes, in contrast to the H^+ signal. Some structure is found that relates to the interfering electronic Rydberg series of the H_2 molecule with $v^+ = 9$ core excitation. This was already found by Kung *et al.* [7] and by Pratt *et al.* [8], where series converging to several rotational quantum states of H_2^+ were observed.

In the present study, excitation occurs via the B–X(17, 0)R(1) transition in the first step, giving access to several s and d Rydberg series in two-photon excitation, with $N^+ = 1$–5 rotational core states. The structure is less pronounced than in the experiments cited above, presumably because the signal includes an incoherent superposition of $J = 1$ and 3 rotational states in the final continuum, for which the series structures are different. Positions of tick marks for electronic Rydberg states in figure 13 are only indicative, obtained from the Rydberg formula and core energies of H_2^+ from [48], without considering quantum defects. In the vicinity of the H^+H^- threshold, only the $N^+ = 1$ series causes a structure in the ion yield that is almost sine shaped, with the phase of the Rydberg series. Suppression of the signal for bound H^+H^- states is due to decay before detection. Although in field-free conditions the lifetime should in theory scale with binding energy as $(-E)^{-3/2}$ (that is, scaling with n^3), a $(-E)^{-2}$ dependence matches much better the observed shape, indicating that stray fields already lead to full ℓ mixing in the states of the heavy H^+H^- Rydberg system.

The signal shape was fitted by the expression for the ion yield I:

$$I \propto \exp\left(-\frac{E^2}{w}\right)\left(1 + a\cos\left(2\pi\left(\frac{R_{H_2}}{E_L - E}\right)^{1/2} + \phi\right)\right), \tag{15}$$

where w is the coefficient governing the energy dependence of the bound state lifetime, E is the binding energy with respect to the H^+H^- dissociation threshold, R_{H_2} is the Rydberg constant for electronic states in the H_2 molecule, $E_L = 150.3\,\mathrm{cm^{-1}}$ is the energy of the $v^+ = 9$, $N^+ = 1$ series limit with respect to the H^+H^- energy and ϕ is 2π times the effective quantum defect.

The fit range is taken from $40\,\mathrm{cm^{-1}}$ below to $36\,\mathrm{cm^{-1}}$ above the H^+H^- limit, which is also taken as a fit parameter, but matches the calculated value within $0.1\,\mathrm{cm^{-1}}$. The fit values for the modulation amplitude and the effective quantum defect are $a = 0.089$ and $\phi/2\pi = -0.05$.

5.2. *Threshold ion-pair spectra*

The purpose of threshold ion-pair production spectroscopy (TIPPS) is to determine the energy of the ion-pair threshold. The technique involves the application of a sequence of two electric fields, a weak discrimination field F_1, which removes 'prompt' ions formed by exciting the continuum, and a strong dissociation field F_2 that afterwards probes the surviving bound ion-pair states. The field F_1 unavoidably also removes very weakly bound states, therefore the field-free threshold energy must be obtained by extrapolation to zero field strength. The accuracy of any straightforward procedure is very limited because TIPPS peaks are typically $10\,\mathrm{cm^{-1}}$ broad; in addition, their shapes change with the electric field (see also [9, 12]), making it difficult to reduce the uncertainty of peak positions to a fraction of the width.

The effects that determine the spectral shape are similar to those pertaining to the weakly bound Rydberg electron in ZEKE and MATI spectroscopy [11, 49] and have also been considered for TIPPS to some extent [12]. Three effects have an influence on the signal: the initial excitation efficiency of the ion-pair configuration, the loss of population in the bound H^+H^- state resulting from the decrease of natural lifetime with increasing binding energy, and the formation of free ion pairs either above threshold or above the saddle point in the electric field F_1. Detection efficiency of the ion-pair state population which has survived to this point may in addition depend on its energy above the new saddle point belonging to the value F_2 of the probe pulse.

Shiell *et al.* [12] showed that in the range of their experimental parameters, the 'red' slope of the spectrum is independent of the electric field, but purely determined by the excitation efficiency and the natural lifetime of the weakly-bound states; F_2 is high enough for the detection efficiency to be essentially unity for the energy region of surviving states. However, this means that the shape does actually depend on the delay of the detection field pulse because bound states are depleted with an energy-dependent time constant. In a similar way, the depletion of bound states on the 'blue' slope as a function of F_1 is also a time-dependent effect.

Extrapolation of the dissociation threshold of H^+H^- to zero field will be more precise with a range of values for the discrimination field F_1 as large as possible, especially since the relevant parameter is only $F_1^{1/2}$. In the present experiment a factor of 20 is covered, compared to a factor of four in [12]. This however requires a variation of the delay of the pulsed field F_2: small F_1 need a long application time to remove the prompt ions, and a late field pulse also helps to sharpen both slopes of the TIPPS peak made up of weakly bound, long-lived states, while for larger F_1 the remaining signal, at higher binding energy, becomes prohibitively small. For these reasons, both sides of the TIPPS signal shape vary with experimental conditions and not only with the high-energy slope as in [12].

5.3. *A fit function for the TIPPS spectra*

Accurate extraction of the saddle point energy from the series of measurements requires a model for the signal shape that takes into account the initial excitation efficiency and the different loss processes during the application of the electric field F_1. For the time-dependent depletion of the H^+H^- population in the TIPPS experiment, a constant decay rate of bound states at energy of E below zero-field threshold is assumed, governing the low-energy ('red') slope of the spectrum, combined with a loss rate due to dissociation above the saddle point determining the high-energy ('blue') slope.

The red-side slope: the process of excitation and population loss below the saddle point is the same as in the case of almost field-free excitation, therefore this part of the TIPPS spectra is given by equation (15), including the parameters of $a = 0.089$ and $\phi = -0.31$, found in that experiment. These are kept fixed in the TIPPS model; for brevity of equations below we define

$$R(E) = 1 + a\cos\left(2\pi\left(\frac{R_{H_2}}{E_L - E}\right)^{1/2} + \phi\right) \qquad (16)$$

representing excitation of the electronic Rydberg series interfering with the H^+H^- channel.

The parameter w governing the slope steepness to the red is left variable, because it depends on the delay of detection t. If one rewrites the exponential factor in equation (15) as $\exp(-t/\tau(E))$, one can substitute from equation (14): $\tau(E) = 59\,\mu s\,(E/cm^{-1})^{-2}$. Defining an energy-scaled decay rate

$$\gamma = 1/(E^2\tau(E)) = 1/(59 \pm 2\,\mu s\,cm^{-2}), \qquad (17)$$

all red-side slopes of the TIPPS spectra are represented, in analogy to equation (15), by

$$I \propto \exp(-E^2\gamma t)R(E), \qquad (18)$$

with t as a fit parameter. Note that t is comparable, but not identical to the trigger delay for the field pulse F_2, due to its slow rise time.

The blue-side slope: in the vicinity of the zero-field dissociation threshold, the slope of a TIPPS spectrum is formed by ion loss due to dissociation above the saddle point, occurring in a way similar to field ionization of electronic Rydberg states. Dissociation rates depend on the lifetimes of individual Stark states, and also on the selection of Stark states in the field ionization process (for an extensive review of the details see [49]). It should be noted that in most experiments the ionization field F_2 is pulsed (PFI), thus transforming Rydberg states that are excited field-free into above-saddle point Stark states; it is then important whether evolution from low to high fields through crossings between the Stark manifolds, which are actually avoided crossings in all systems but the hydrogen atom, is diabatic or adiabatic. In the present experiment however, different from earlier TIPPS experiments [10, 12, 15, 50], excitation occurs while the discrimination field F_1 is already present. Therefore all Stark states that may be involved

in above-saddle point population loss are at the excitation energy, a situation that resembles adiabatic evolution in PFI.

In view of the high quantum numbers we do not determine the population loss in terms of lifetimes of individual Stark states. Instead we make a semiclassical approximation by considering all classical trajectories, associated with the outgoing wave of H^+H^- formation at a given energy, in the combined Coulomb and static-field potential and assign them a loss probability of 1 or 0, depending on whether they either go through the saddle point or return to the centre. The angular distribution of outgoing trajectories is assumed to be isotropic, which would be exact only for a $J = 0$ excited configuration, but is a reasonable approximation for the combination of $J = 1$ and 3 final states, with different m quantum numbers, in the present scheme. The fraction of solid angle, from which trajectories go through the saddle point region, equalling the 'immediate' dissociation probability of a H^+H^- state at energy E in between the saddle point and the zero-field threshold, is thus given by [51]

$$S(E, F) = 1 - (E/E_s)^2, \tag{19}$$

where $-E_s$ is the electrostatic saddle point energy with respect to the zero-field threshold,

$$E_s(F) = \frac{-6.12\,\mathrm{cm}^{-1}}{(\mathrm{V\,cm}^{-1})^{1/2}} F^{1/2}. \tag{20}$$

Outside the range of $E_s < E < 0$ where equation (19) holds, $S(E)$ can be extended by

$$\begin{aligned} S(E < E_s) &= 0, \\ S(E > 0) &= 1. \end{aligned} \tag{21}$$

There is a sharp change of the slope at E_s, therefore the fit function must include explicitly the smoothing effect of the instrument function, to prevent unphysical convergence of the edge to a noise peak. This is most naturally done by convolution with a Gaussian, with a width that we keep constant at $\Delta_G = 0.5\,\mathrm{cm}^{-1}$, accounting for laser bandwidth as well as differences of saddle point energies in the interaction region due to stray fields:

$$\bar{S}(E, F) = \frac{1}{(2\pi\Delta_G)^{1/2}} \int_{-\infty}^{+\infty} S(E',\, F)\, \exp \frac{(E' - E)^2}{2\Delta_G^2}\, \mathrm{d}E'. \tag{22}$$

At high-field strengths the signal in the continuum as well as in the saddle point region drops sharply to zero when the delay of F_2 is sufficient to let free ions reach the opposite plate beforehand. In contrast, some fraction of the ions remains detectable, whatever the delay time, for small discrimination fields. Similar effects were observed in ZEKE-PFI spectroscopy and were attributed to partial shielding of the field by the ion-cloud [39]. The ion detection probability $p(E, F_1)$ after application of discrimination field F_1 is thus related to the saddle-point dissociation function $\bar{S}$ for immediate decay via

$$p(E, F_1) = 1 - f\bar{S}(E, F_1) \tag{23}$$

with a discrimination efficiency factor f.

In addition to this prompt ion-pair field dissociation, it is necessary to include a delayed population loss, making the ion-detection probability function $p(E)$ time dependent. Unfortunately this delayed loss cannot be combined with the natural decay into a unique ion-signal loss rate as a function of energy, because decay of a bound H^+H^- system connected to the natural lifetime reduces the detection probability p to zero, while decay via field dissociation only reduces p to f, which is not determined by the model.

The energy and time dependence of this process is derived from its relation to elastic scattering between orbit angles upon close approach of H^+ and H^-, or in other terms, with different quantum defects of angular momentum channels. Both classical and quantum mechanics predict for scattering in a pure Coulombic potential centre that the angular distribution before and after scattering be identical; any H^+H^- population that survived the first encounter with the saddle point region would also survive the subsequent ones. One might expect that at each close encounter of the ion-pair, the angular distribution is changed into an isotropic one as after initial excitation, but this is not supported by the observed line shapes. Instead, there appears to be a finite, energy-dependent probability for such redistribution to occur; the *ansatz* is that it is given by the probability that upon close approach of the classical orbit, some critical distance is reached. This is equivalent to a fixed number N of angular momentum channels having non-vanishing (and suitably distributed) quantum defects. The rate of close encounters of the ions on the classical trajectory is given by the inverse Kepler orbit time for the given principal quantum number as

$$T_n^{-1} = \frac{M}{2\pi n^3 \tau_0} = \frac{ME_h}{n^3 h} = \frac{2cMR_\infty}{n^3} \tag{24}$$

(see tables 2 and 3).

Due to the linear time evolution of angular momentum, the system is equally likely to be in each of the $n - 1 \approx n$ channels at the encounter, therefore each

channel contributes to the redistribution rate with a fraction of $1/n$ of the value given in equation (24). Written as a function of binding energy $E = -MR_\infty/n^2$, this results in an energy-scaled redistribution rate per channel, defined as $\gamma_r = 1/(T_n n E^2)$, of

$$\gamma_r = \frac{2cMR_\infty}{n^4E^2} = \frac{2c}{MR_\infty} = 594.8\ \frac{\mathrm{s}^{-1}}{\mathrm{cm}^{-2}}. \qquad (25)$$

The average dissociation efficiency due to trajectories crossing the saddle point region after angular redistribution is the same as after initial excitation and therefore equals $\bar{S}(E)$. The fraction of H^+H^- systems that survived the initial direct loss, $1-\bar{S}$, thus further decreases in time with a factor $\exp(-N\gamma_r E^2\bar{S}t)$. The ions from the non-surviving fraction are then removed by the discrimination field F_1 with efficiency f; the remaining fraction, i.e. either not dissociated or dissociated but not removed, defines the overall detection probability function

$$p = 1 - f\big(1 - (1-\bar{S})\exp(-N\gamma_r E^2\bar{S}t)\big), \qquad (26)$$

which in the case of $f = 1$ reduces to

$$(1-\bar{S})\exp(-N\gamma_r E^2\bar{S}t), \qquad (27)$$

while matching equation (23) in the case of $t = 0$. The most interesting part of p is for $E_s < E < 0$, while below the saddle point $E_s(F_1)$, p becomes unity, and above the zero-field threshold, $p = 1 - f$.

Finally the complete model function for the TIPPS ion yield becomes

$$I(E, F_1, N, t) \propto R(E)\exp(-E^2\gamma t)p(E, F_1, N, t). \qquad (28)$$

5.4. *Extrapolation to zero-field limit*

Individual scans with different discrimination fields F_1 and delays of the pulsed field F_2 are fitted with the function given in equation (28). Physically meaningful fit parameters, next to the signal background and the intensity scaling factor, are only the zero point for the energy E, the effective detection delay t and the prompt-ion discrimination efficiency f. The global number of angular-momentum redistributing channels was set to a fixed value of $N = 80$, providing a good representation of all spectra; inclusion as a fit parameter leads to scatter between about 50 and 120, but also multiple 'best fits' leading to rather different N values for a single spectrum.

Figure 14 shows a TIPP spectrum with a fit to the model function. Due to the use of F_1 as a fixed parameter in equation (28), the fit result provides values for the saddle point energy and the zero-field threshold at the same time, related by equation (20), which are indicated in the figure. The uncertainty of F_1 due to space charge effects is estimated to be $0.1\ \mathrm{V\,cm^{-1}}$, based on the result from the wave packet oscillation experiment that the frequency changes slightly when the field orientation is changed (see figure 8). The uncertainty of the energy found in the individual fits is estimated from the fit quality.

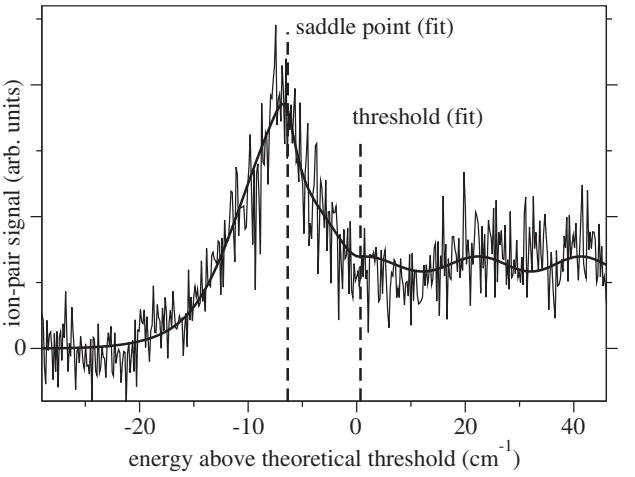

Figure 14. Measured field-dissociation spectrum in the TIPPS configuration at a DC voltage of $1.2\ \mathrm{V\,cm^{-1}}$ and a delayed pulsed field of $50\ \mathrm{V\,cm^{-1}}$; the solid line results from a fit with the model function as described in the text.

Based on spectra recorded at different F_1, the fitted saddle-point energies are extrapolated to $F_1 = 0$ in figure 15 with a weighted linear fit, with weights based on both field and energy uncertainty. Alternatively, the

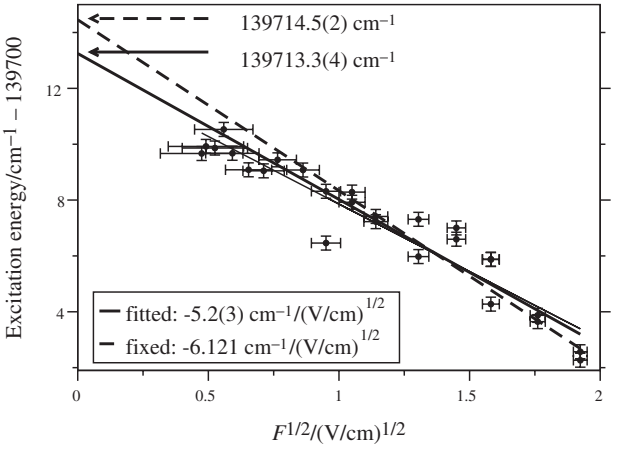

Figure 15. H^+H^- saddle point energies, as obtained from model fits to the TIPPS measurements for various DC electric fields, and extrapolation to zero field. The uncertainties given for the fit parameters are the variances pertaining to the fit, not including the experimental uncertainties.

threshold-energy values resulting from individual TIPPS fits can be extrapolated to $F_1 = 0$, which is equivalent to fitting the saddle-point energies to a straight line with a fixed slope of $6.12\,\mathrm{cm}^{-1}\,(\mathrm{V\,cm}^{-1})^{-1}$, which is also shown in figure 15. Ideally, both fits should coincide; the continuous presence of F_1 during excitation, until the detection field F_2 is switched, rules out that diabatic versus adiabatic Stark state dynamics changes the saddle point lowering coefficient.

The real field strength for the ions could also be affected by space or surface charge effects, which are held responsible for the incomplete ion removal at small F_1 strengths [39], but these should usually make the real field smaller than the apparently measured value, not larger than would be necessary to explain the observed discrepancy. In any case of an incorrect F_1 value, the representation of the spectral shape by the model function would be slightly affected, because the position of the saddle point with respect to the Rydberg-structure modulation $R(E)$ would be slightly shifted, thus creating an additional uncertainty for the saddle-point energy.

Without an advanced control of the discrimination field, we take as the result for the H^+H^- dissociation threshold a value that spans both extrapolation values and their respective uncertainties: $139713.8 \pm 0.9\,\mathrm{cm}^{-1}$. This result is consistent with the literature, but not more precise than previous measurements in spite of the larger range of discrimination field values [12]. It should however be pointed out that the discrepancy of slopes between the two ways of extrapolation would not even have shown up with a more restricted set of field values.

6. Discussion of some outstanding issues

6.1. *Resolving the heavy Rydberg series*

The observation of the lifetimes of H^+H^- bound Rydberg states has an impact on the possibility of observing individual quantum states, either in an electric field or field-free. In an electric field above the Inglis–Teller limit, where Stark manifolds of different n overlap, the average state density is $0.5n^3(n+1) \approx 0.5n^4$ in atomic units, or $4.96 \times 10^{-9} n^4$ states per cm^{-1} for H^+H^-, corresponding to an average level spacing of $2.02 \times 10^8\, n^{-4}\,\mathrm{cm}^{-1}$. On the other hand, the natural energy width of a Stark state, derived from the experimental lifetime as $\delta\nu = \Gamma/2\pi = 1/2\pi\tau$, is on average $(3.1 \pm 1.1) \times 10^{19} n^{-4}\,\mathrm{Hz}$ or $(10 \pm 3.5) \times 10^8 n^{-4}\,\mathrm{cm}^{-1}$. This means that the Stark states everywhere in the manifold are expected to overlap fivefold on average within their natural widths, making it impossible to resolve them in a frequency-scanning spectroscopy experiment.

Spectrally resolving the consecutive heavy Rydberg states in zero electric field might be possible, provided there are low-J states in some range of binding energy for which the lifetimes are considerably longer than the respective Kepler orbit times. But even if all core-penetrating states are short-lived, the series should be present as an oscillation on each decay channel, due to interference of direct ionization and dissociation with the respective indirect process via the H^+H^- state, with decay products in the same quantum state. In both cases, observations are only feasible in lower energy regions than examined in this paper, where the requirement of suppressing the stray electric fields below the Inglis–Teller limit $(1.5 \times 10^{15}\,\mathrm{V\,cm}^{-1}\,n^{-5}$, equalling $0.05\,\mathrm{V\,cm}^{-1}$ for $n = 2000$) is less tight.

6.2. *Oscillator strength for exciting ion-pair states*

Although photodissociation of H_2 into H^+H^-, by schemes involving one or several photons, has been investigated over the years, little is known about the exact nature of the highly excited molecular states that finally lead to ion-pair formation. Pure heavy Rydberg states with high principal quantum number have a wave function with virtually all density located at extremely large internuclear separation; like in electronic Rydberg systems, no fundamental change of the short-range wave function is to be expected at the threshold between asymptotically bound and unbound ion-pair states. Hence no Franck–Condon overlap is available for excitation to the pure heavy-Rydberg character, neither from the ground state nor from any optically excited valence or Rydberg states, which are confined to relatively short internuclear distance. Optical excitation must therefore be followed by some internal evolution into the ion-pair configuration.

Ion-pair production spectra of Chupka *et al.* [6], Kung *et al.* [7] and Pratt *et al.* [8], as well as in the present experiment (figure 13), show a prominent structure that can be assigned as one or more electronic Rydberg series of H_2 with excited core $v^+ = 9$, which are distorted by still unidentified 'interlopers'. In the cited studies, where the final states are in one well-known J state due to optical selection rules, the structure in the H^- spectra has minima close to zero, as is typical for a single continuum interacting with bound states. We chose a different excitation scheme such that contributions with $J = 2$–4 are present, with different positions of the minima, leading to a smoother spectrum favourable for the TIPPS experiment as well as for excitation of wave packets at arbitrarily chosen energies.

Unfortunately, it is next to impossible to make statements on the role of different states that form the observed complex resonances in the process of ion-pair

formation, without a detailed model describing these states. This can be deduced from the theoretical analysis by Giusti-Suzor and Lefebvre-Brion [52] for the simplified case of an optically excited complex resonance composed of one Rydberg series, one additional discrete state and one continuum; while direct optical excitation is assumed to be absent, optical dipole amplitude to all bound states is included, as well as interactions between all three entities. There are several striking results: the Rydberg series is prominent even when its oscillator strength is small; there is always a clear effect of the interloper, even when its oscillator strength is zero; the centre and width of the region in the Rydberg series that appears to be perturbed do not match the eigen-energy and the natural width of the interloper.

The situation in H_2 is still more complicated due to other autoionization and predissociation channels to which coupling appears to be even stronger than to the H^+H^- configuration, as we observe the corresponding products in larger quantity than excited H^+H^- systems. It should however be emphasized that the presence of more continua may further shorten lifetimes of the doorway states and thereby smooth the H^+H^- excitation spectrum, but in no circumstances can enhance the transition probability at any wavelength, compared to the model with one continuum. Therefore ion-pair excitation in other molecules with fewer competing decay channels should in principle be more efficient.

The issue of oscillator strength touches upon the question as to what is molecule-specific in the H^+H^- heavy Rydberg states and what is general. To a first approximation atomic Rydberg states are all alike insofar as the series converging to the first ionization limit are concerned; a sequence of states defined by the Rydberg formula, which can only decay radiatively. We note again that all atoms are associated with the same Rydberg constants; the reduced-mass effect is minute. Atom-specific effects only play a role when doubly-excited states energetically coincide with the series of Rydberg states. Heavy Rydberg states in molecular ion-pair systems are different from each other because they all have widely varying Rydberg constants. More importantly the dense series of heavy Rydberg states always coincide with dissociative and autoionizing continua and these interactions determine a material constant: the scaled lifetime is here determined at $\tau = (5.8 \pm 2.0) \times 10^{-21}\,\mathrm{s}\,n^4$ for the specific case of the H^+H^- system. For not many ion-pair systems a scaled lifetime has been determined, hence no general statements can be made as to whether this value is large or small. In the case of ICl lifetimes of 5 μs were observed at energies $50\,\mathrm{cm}^{-1}$ below threshold [13]. The halogen and interhalogen molecules are special, having their ion-pair dissociation threshold below the ionization potential, hence their lifetimes are not shortened by autoionization. This makes the halogen molecules attractive systems to detect oscillating heavy Rydberg wave packets.

Experimentally we have observed strong decay of the heavy Rydberg states, for which several ionization and dissociation continua are accessible for different numbers of angular momentum channels, making it difficult to determine their relative importance without further experiments in which decay products are probed specifically. Especially, the $H(n = 4) + H(n = 1)$ dissociative continuum has been found to be strong in optical excitation of H_2 at the H^+H^- energy, but only a few J components of H^+H^- can actually decay into this channel. It may well be that in other ion-pair systems, even the ones where the ion-pair limit is above the IP, the additional decay channels are weaker. This would cause the coherent wave packets to live longer, which would have the beneficial effect that their properties could be studied in more detail.

6.3. *Transition quantum to classical*

The high quantum numbers of the states of H^+H^- investigated here suggest that the system might approach macroscopic, classical behaviour, but it is well known since Schrödinger's investigation of the transition to classical physics at large quantum numbers [53] that this is a necessary but not sufficient condition. For the special case of the harmonic oscillator, Schrödinger shortly afterwards solved the problem of finding states with uncertainties of observables that do not increase with time, now called coherent states [54]; but the quantum-classical boarder in general has remained a productive field of research until today. An overview of the classical limit of the Coulomb system, which is the relevant background for the H^+H^- system, is given by Bluhm *et al.* [55]; it is pointed out that in the Coulomb problem, exact coherent states do not exist, but under certain conditions wave packets can move close to a classical trajectory.

As an extreme example for an $1/r$ potential, one may consider the Earth–Sun system with GM_1M_2 substituted for $Ze^2/4\pi\epsilon_0$ in the Coulomb potential, leading to the gravitational analogue of the Rydberg constant of $R_g = 1.7 \times 10^{182}\,\mathrm{J}$, while the principal quantum number for the orbit is $n = 3 \times 10^{74}$, with level spacings as small as $\Delta E = 2 \times 10^{-41}\,\mathrm{J}$. A wave packet of circular Rydberg states centred at the Earth's principal quantum number, with spread $\Delta n = n^{1/2}$, would have an energy uncertainty of $\Delta E = 0.02\,\mathrm{mJ}$, a radial position uncertainty of $\Delta R = 2.1 \times 10^{-26}\,\mathrm{m}$, an angular uncertainty of $\Delta\phi = 2.9 \times 10^{-38}\,\mathrm{rad}$ corresponding to an angular position uncertainty on Earth's orbit of $2.7 \times 10^{-26}\,\mathrm{m}$,

and an increase of the angular uncertainty with time due to wave packet dispersion of $d\Delta\phi/dt = 2.1 \times 10^{-44}\,\mathrm{rad\,s^{-1}}$ corresponding to an increase of orbital position uncertainty of $6.2 \times 10^{-25}\,\mathrm{m\,yr^{-1}}$.

The classical limit of the Coulomb system has to be distinguished from semi-classical treatments of Rydberg states, like closed-orbit theory, involving classical orbits in the Coulomb potential for determining the oscillator strength for Rydberg states in electric fields [56]. In fact the system remains fully quantum-mechanical, and the treatment gives a relationship between the classical dynamics and the density of states [57]; the latter can be investigated experimentally by 'scaled energy spectroscopy', where excitation energy and external fields are varied together such that the corresponding classical dynamics remains unaltered, except for a scale factor [58]. Particular interest was raised in the problem of Rydberg states in magnetic fields, because the classical dynamics of the system is chaotic [59]; the quantum mechanical fingerprint associated with this behaviour is that the nearest-neighbour level separation follows a Wigner distribution [60, 61]. This feature underlies the influence of an ionic core, as was first observed in the Stark spectrum of lithium [62].

Close-to-classical behaviour of wave packets in the Coulomb system can occur independently for different degrees of freedom in one single system, because these types of motion are separable [55]. This has also been investigated experimentally: Ten Wolde *et al.* observed purely radially oscillating wave packets of Rydberg electrons [18], but also wave packets evolving in angular momentum in an electric field [19]; similar observations were made by Yeazell and co-workers [20, 21]. Comparable effects of radial nuclear motion on a non-Coulombic potential in NO were found by Fielding and co-workers [63], putting their observation also in a wider perspective of wave packets of nuclear motion in general. A signature of angular wave packets was also observed [64, 65]. The possibility of non-classical superpositions of nuclear wave packets was shown experimentally by Vrakking *et al.* [66] and by Noel and Stroud [67], which illustrates that high quantum numbers do not necessarily lead to classical behaviour.

The ion-pair states, as discussed here, form an extended platform to study the problem of the quantum-to-classical transition in the Coulomb system, with easy access to larger quantum numbers due to the higher mass compared to Rydberg electrons. In the circumstances in which H^+H^- wave packets are investigated in this paper, the radial motion is purely quantum-like, while the angular momentum evolution has the classical signature of keeping a very small spread from the preparation through the entire lifetime of the system.

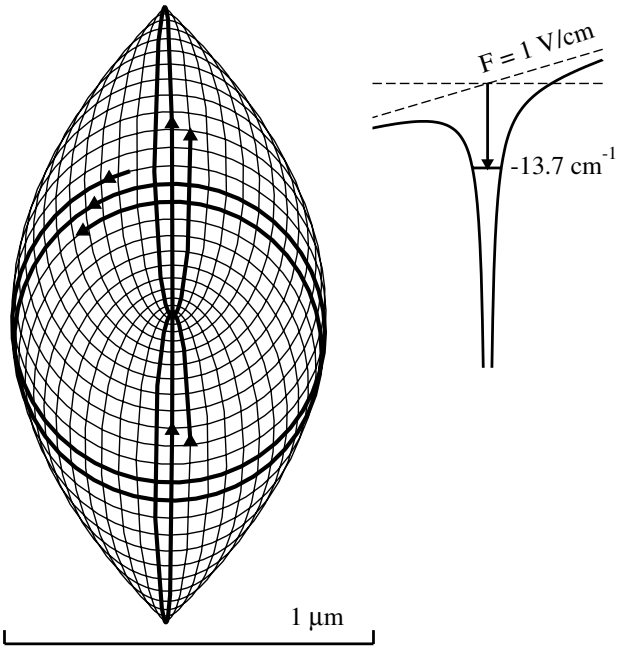

Figure 16. Classical closed orbit of the reduced H^+H^- system in an electric field. The extension of the wave packet around its classical position in the radial dimension is indicated by an arrow at three different times. The spread in the initial angle is essentially 2π because J is sharp; only one selected angle $\pi/2$ with the field axis is displayed.

To illustrate this point, figure 16 shows the classical orbit of H^+H^- for typical experimental parameters, with the initial angle chosen perpendicular to the electric field. The correct representation of the experimentally prepared wave packet includes all possible angles that belong to the initial angular momentum wave function. The centre of a close-to-classical wave packet follows such a trajectory, but shows a certain spread due to the uncertainty relation. The extension of the wave packet along the trajectory, due to the time uncertainty of its creation, is indicated by bold arrows at three different times of the wave packet evolution; at any moment the entire accessible radial range is covered, while the spread due to dispersion is negligible over the time of an entire orbit. The angular momentum is sharply defined at all times, due to selection rules at formation combined with little dispersion of the Stark states; on the other hand, the wave packet has no defined angular coordinate, which is especially far from classical.

7. Conclusion

In conclusion, we have observed coherent time evolution of wave packets in the heavy Rydberg system H^+H^- in an electric field on time scales of 1 μs, only

limited by excited state lifetimes for large binding energy and dispersion of strongly overlapping Stark manifolds at small binding energy. Observed coherence times in H^+H^- are 3–4 orders of magnitude longer than for electronic wave packets [68]. It is shown that the physical laws governing the series of quantum states below an ion-pair limit are the same as those for electronic Rydberg states, when appropriate mass-scaling is applied. Hence, the H^+H^- system can be described as a hydrogen atom, where the negatively charged electron is replaced by a pointlike H^- particle. Such heavy Rydberg states might be interesting for storage of quantum information, as recently realized in electronic Rydberg states [69]. Controlled changes of the electric field on this time scale are feasible, opening the possibility of manipulating the coherent evolution of wave packets in real-time. For this purpose it would be useful to find ion-pair systems with longer-lived heavy Rydberg states. Heavy Rydberg states are at the boundary of quantum to classical behaviour and form model systems to investigate the transition between the two regimes.

Acknowledgements

Financial support from the Netherlands Foundation for Fundamental Research of Matter (FOM) and from the Space Research Organization Netherlands (SRON) is gratefully acknowledged. ER acknowledges support from the European Community in the form of a Marie Curie individual fellowship at LAC (HPMF-CT-2000-00964). This work was further supported by the EU program Access to Research Infrastructures, Contract no. HPRI-CT-1999-00064.

References

[1] T.F. Gallagher, *Rydberg Atoms*, Cambridge University Press, Cambridge (1994).
[2] C. Jungen, U. Even, M.S. Child. *Adv. Chem. Phys.*, **101,** 701 (1997).
[3] R.A.L. Smith, J.R.R. Verlet, H.H. Fielding. *Phys., Chem. Chem. Phys.*, **5,** 3567 (2003).
[4] T.P. Softley. *Int. Rev. Phys. Chem.*, **23,** 1 (2004).
[5] S.H. Pan, F.H. Mies. *J. chem. Phys.*, **89,** 3096 (1988).
[6] W.A. Chupka, P.M. Dehmer, W.T. Jivery. *J. chem. Phys.*, **63,** 3929 (1975).
[7] A.H. Kung, R.H. Page, R.J. Larkin, Y.R. Shen, Y.T. Lee. *Phys. Rev. Lett.*, **56,** 328 (1986).
[8] S.T. Pratt, E.F. McCormack, J.L. Dehmer, P.M. Dehmer. *Phys. Rev. Lett.*, **68,** 584 (1992).
[9] J.D.D. Martin, J.W. Hepburn. *Phys. Rev. Lett.*, **79,** 3154 (1997).
[10] J.D.D. Martin, J.W. Hepburn. *J. chem. Phys.*, **109,** 8139 (1998).
[11] K. Müller-Dethlefs, E.W. Schlag. *Annu. Rev. Phys. Chem.*, **42,** 109 (1991).
[12] R.C. Shiell, X.K. Hu, Q.C.J. Hu, J.W. Hepburn. *Faraday Discuss.*, **115,** 331 (2000).
[13] S. Wang, K.P. Lawley, T. Ridley, R.J. Donovan. *Faraday Discuss.*, **115,** 345 (2000).
[14] T. Ridley, M. De Vries, K.P. Lawley, S. Wang, R.J. Donovan. *J. chem. Phys.*, **117,** 7117 (2002).
[15] R.C. Shiell, X.K. Hu, Q.C.J. Hu, J.W. Hepburn. *J. phys. Chem.* A, **104,** 4339 (2000).
[16] E. Schrödinger. *Naturwissenschaften*, **28,** 664 (1926).
[17] G. Alber, H. Ritsch, P. Zoller. *Phys. Rev.* A, **34,** 1058 (1986).
[18] A. Ten Wolde, L.D. Noordam, A. Lagendijk, H.B. van Linden van den Heuvell. *Phys. Rev. Lett.*, **61,** 2099 (1988).
[19] A. Ten Wolde, L.D. Noordam, A. Lagendijk, H.B. van Linden van den Heuvell. *Phys. Rev.* A, **40,** 485 (1989).
[20] J.A. Yeazell, C.R. Stroud. *Phys. Rev. Lett.*, **60,** 1494 (1988).
[21] J.A. Yeazell, M. Mallalieu, J. Parker, C.R. Stroud. *Phys. Rev.* A, **40,** 5040 (1989).
[22] M. Dantus, R.M. Bowman, A.H., Zewail. *Nature*, **343,** 737 (1990).
[23] A.H. Zewail. *Angew. Chem.*, **39,** 2587 (2000).
[24] G.M. Lankhuizen, L.D. Noordam. *Phys. Rev. Lett.*, **76,** 1784 (1996).
[25] E. Reinhold, W. Ubachs. *Phys. Rev. Lett.*, **88,** 013001 (2002).
[26] E. Reinhold, W. Hogervorst, W. Ubachs. *Phys. Rev. Lett.*, **78,** 2543 (1997).
[27] A. De Lange, W. Hogervorst, W. Ubachs, L. Wolniewicz. *Phys. Rev. Lett.*, **86,** 2988 (2001).
[28] L. Wolniewicz, G. Staszewska. *J. molec. Spectrosc.*, **220,** 45 (2003).
[29] T. Detmer, P. Schmelcher, L.S. Cederbaum. *J. chem. Phys.*, **109,** 9694 (1998).
[30] G. Staszewska, L. Wolniewicz. *J. molec. Spectrosc.*, **212,** 208 (2002).
[31] J.C.J. Koelemeij, A. De Lange, W. Ubachs. *Chem. Phys.*, **287,** 349 (2003).
[32] D. Shiner, J.M. Gilligan, B.M. Cook, W. Lichten. *Phys. Rev.* A, **47,** 4042 (1993).
[33] A. De Lange, E. Reinhold, W. Ubachs. *Phys. Rev.* A, **65,** 064501 (2002).
[34] E.E. Eyler, N. Melikechi. *Phys. Rev.* A, **48,** R18 (1993).
[35] A. Balakrishnan, V. Smith, B.P. Stoicheff. *Phys. Rev.* A, **49,** 2460 (1994).
[36] Y.P. Zhang, C.H. Cheng, J.Y. Kim, J. Stanojevic, E.E. Eyler. *Phys. Rev. Lett.*, **92,** 203003 (2004).
[37] W.R. Johnson, G. Soff. *At. Data Nucl. Data Tables*, **33,** 405 (1985).
[38] K.R. Lykke, K.K. Murray, W.C. Lineberger. *Phys. Rev.* A, **43,** 6104 (1991).
[39] F. Merkt, R.N. Zare. *J. chem. Phys.*, **101,** 3495 (1994).
[40] H.A. Bethe, E.E. Salpeter. *Quantum Mechanics of One- and Two-Electron Atoms*, Plenum Publishing, New York (1977).
[41] E. Reinhold, A. De Lange, W. Hogervorst, W. Ubachs. *J. chem. Phys.*, **109,** 9772 (1998).
[42] C.R. Scheper, C.A. De Lange, A. De Lange, E. Reinhold, W. Ubachs. *Chem. Phys. Lett.*, **312,** 131 (1999).
[43] M.J.J. Vrakking, Y.T. Lee. *J. chem. Phys.*, **102,** 8818 (1995).

[44] E. Reinhold, W. Hogervorst, W. Ubachs. *J. chem. Phys.*, **112,** 10754 (2000).
[45] T. Tanabe, I. Katayama, H. Kamegaya, K. Chida, Y. Arakaki, T. Watanabe, M. Yoshizawa, M. Saito, Y. Haruyama, K. Hosono, K. Hatanaka, T. Honma, K. Noda, S. Ohtani, H. Takagi. *Phys. Rev. Lett.*, **75,** 1066 (1995).
[46] D. Zajfman, Z. Amitay, M. Lange, U. Hechtfischer, L. Knoll, D. Schwalm, R. Wester, A. Wolf, X. Urbain. *Phys. Rev. Lett.*, **79,** 1829 (1997).
[47] W. Zong, G.H. Dunn, N. Djurić, M. Larsson, C.H. Greene, A. Al-Khalili, A. Neau, A.M. Dekatch, L. Vikor, W. Shi, A. Le Padellec, S. Rosén, H. Danared, M. Af Ugglas. *Phys. Rev. Lett.*, **83,** 951 (1999).
[48] R.E. Moss. *Molec. Phys.*, **80,** 1541 (1993).
[49] F. Merkt. *Ann. Rev. Phys. Chem.*, **48,** 675 (1997).
[50] Q.J. Hu, T.C. Melville, J.W. Hepburn. *J. chem. Phys.*, **119,** 8938 (2003).
[51] M.W. Beims, V. Kondratovich, J.B. Delos. *Phys. Rev.* A, **62,** 043401 (2000).
[52] A. Giusti-Suzor, H. Lefebvre-Brion. *Phys. Rev.* A, **30,** 3057 (1984).
[53] E. Schrödinger. *Naturwissenschaften*, **14,** 137 (1926).
[54] E. Schrödinger. *Naturwissenschaften*, **14,** 664 (1926).
[55] R. Bluhm, V.A. Kostelecký, B. Tudose. *Phys. Rev.* A, **53,** 937 (1996).
[56] M.L. Du, J.B. Delos. *Phys. Rev.* A, **38,** 1896 (1988).
[57] M.C. Gutzwiler. *J. math. Phys.*, **12,** 343 (1971).
[58] A. Holle, G. Wiebusch, J. Main, B. Hager, H. Rottke, K.H. Welge. *Phys. Rev. Lett.*, **57,** 2789 (1986).
[59] H. Friedrich, D. Wintgen. *Phys. Rep.*, **183,** 37 (1989).
[60] D. Delande, J.C. Gay. *Phys. Rev. Lett.*, **57,** 2006 (1986).
[61] K. Karremans, W. Vassen, W. Hogervorst. *Phys. Rev. Lett.*, **81,** 4843 (1998).
[62] M. Coutney, H. Jiao, N. Spellmeyer, D. Kleppner. *Phys. Rev. Lett.*, **62,** 893 (1989).
[63] R.A.L. Smith, J.R.R. Verlet, H.H. Fielding. *Phys. Chem. Chem. Phys.*, **5,** 3567 (2003).
[64] R.S. Minns, R. Patel, J.R.R. Verlet, H.H. Fielding. *Phys. Rev.* A, **91,** 243601 (2003).
[65] R.S. Minns, J.R.R. Verlet, L.J. Watkins, H.H. Fielding. *J. Chem. Phys.*, **119,** 5842 (2003).
[66] M.J.J. Vrakking, D.M. Villeneuve, A. Stolow. *Phys. Rev.* A, **54,** R37 (1996).
[67] M.W. Noel, C.R. Stroud. *Phys. Rev. Lett.*, **77,** 1913 (1996).
[68] J.B.M. Warntjes, C. Wesdorp, F. Robicheaux, L.D. Noordam. *Phys. Rev. Lett.*, **83,** 512 (1999).
[69] J. Ahn, T.C. Weinacht, P.H. Bucksbaum. *Science*, **287,** 463 (2000).